

# Identification of Ubiquinol Binding Motifs at the Q<sub>o</sub>-Site of the Cytochrome bc<sub>1</sub> Complex

Angela M. Barragan,<sup>†,‡</sup> Antony R. Crofts,<sup>¶,§</sup> Klaus Schulten,<sup>†,‡</sup> and Ilia A. Solov'yov\*,||,⊥

<sup>†</sup>Department of Physics, University of Illinois at Urbana–Champaign, 1110 W. Green Street, Urbana, Illinois 61801, United States

<sup>‡</sup>Beckman Institute for Advanced Science and Technology, University of Illinois at Urbana–Champaign, 405 N. Mathews Ave, Urbana, Illinois 61801, United States

<sup>¶</sup>Department of Biochemistry, University of Illinois at Urbana–Champaign, 600 S. Mathews Ave, Urbana, Illinois 61801, United States

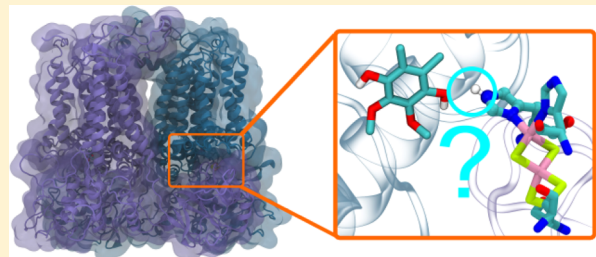
<sup>§</sup>Center for Biophysics and Computational Biology, University of Illinois at Urbana–Champaign, 607 S. Mathews Ave, Urbana, Illinois 61801, United States

<sup>||</sup>Department of Physics, Chemistry and Pharmacy, University of Southern Denmark, Campusvej 55, DK-5230 Odense M, Denmark

<sup>⊥</sup>A. F. Ioffe Physical-Technical Institute, Politehnicheskaya 26, 194021 St. Petersburg, Russia

## S Supporting Information

**ABSTRACT:** Enzymes of the bc<sub>1</sub> complex family power the biosphere through their central role in respiration and photosynthesis. These enzymes couple the oxidation of quinol molecules by cytochrome c to the transfer of protons across the membrane, to generate a proton-motive force that drives ATP synthesis. Key for the function of the bc<sub>1</sub> complex is the initial redox process that involves a bifurcated electron transfer in which the two electrons from a quinol substrate are passed to different electron acceptors in the bc<sub>1</sub> complex. The electron transfer is coupled to proton transfer. The overall mechanism of quinol oxidation by the bc<sub>1</sub> complex is well enough characterized to allow exploration at the atomistic level, but details are still highly controversial. The controversy stems from the uncertain binding motifs of quinol at the so-called Q<sub>o</sub> active site of the bc<sub>1</sub> complex. Here we employ a combination of classical all atom molecular dynamics and quantum chemical calculations to reveal the binding modes of quinol at the Q<sub>o</sub>-site of the bc<sub>1</sub> complex from *Rhodobacter capsulatus*. The calculations suggest a novel configuration of amino acid residues responsible for quinol binding and support a mechanism for proton-coupled electron transfer from quinol to iron–sulfur cluster through a bridging hydrogen bond from histidine that stabilizes the reaction complex.



## INTRODUCTION

The biosphere is sustained by chemiosmotic circuits, driven by light (in photosynthesis) or chemical potential difference (in respiration), through which electron transfer reactions coupled to proton transfer across a cellular membrane maintain the proton gradient that drives cellular metabolism through synthesis of adenosine triphosphate (ATP), transport of ions and metabolites, and other processes.<sup>1–4</sup> Specialized proteins and protein complexes facilitate electron transfer between distinct electron donor and acceptor sites. In the case of cellular respiration or photosynthesis, a multiprotein enzyme that drives proton translocation across the cellular membrane while performing electron transfer is the cytochrome bc<sub>1</sub> complex.<sup>5,6</sup> The overall reaction of the bc<sub>1</sub> complex, also referred to as the Q-cycle, results in the net oxidation of two quinol (QH<sub>2</sub>) molecules with the release of four protons to the positive side of the membrane (or intermembrane space in the case of mitochondria), and reduction of one quinone (Q) with uptake of two protons from the negative side.<sup>7</sup>

Numerous bc<sub>1</sub> complex structures have been resolved through X-ray crystallographic methods, namely bovine,<sup>8</sup> chicken,<sup>4</sup> yeast,<sup>9</sup> and bacterial<sup>10</sup> ones. The functional core of bacterial and mitochondrial bc<sub>1</sub> complexes consists of a dimeric protein arrangement, where each monomer contains one cytochrome b (cyt. b), one cytochrome c<sub>1</sub> (cyt. c<sub>1</sub>), and one iron–sulfur protein (ISP) subunit, as illustrated in Figure 1a. These subunits bind several prosthetic groups that are involved in electron transfer through the bc<sub>1</sub> complex and, therefore, are crucial for the Q-cycle. In particular, the cyt. b subunit contains two iron-containing heme b groups, the cyt. c<sub>1</sub> subunit contains a heme c group, and the ISP subunit contains an Fe<sub>2</sub>S<sub>2</sub> cluster, as shown in Figure 1b.

Each monomer of the bc<sub>1</sub> complex (see Figure 1a) includes two active sites that govern the functional capabilities of the entire complex and are referred to as the Q<sub>o</sub>- and Q<sub>c</sub>-sites (see

Received: October 3, 2014

Revised: November 4, 2014

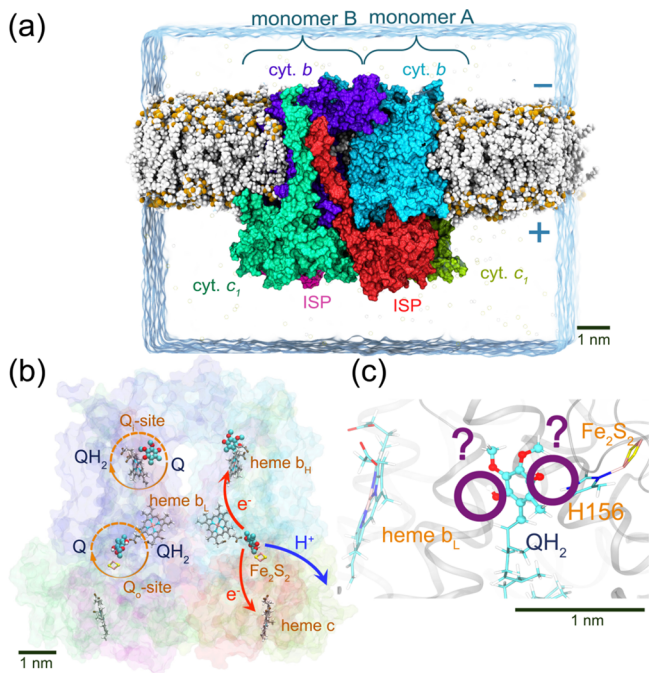


**Figure 1.** *bc<sub>1</sub>* complex from *Rhodobacter capsulatus*. (a) The studied molecular system consists of a lipid bilayer membrane, water molecules, ions, and the six protein subunits forming the homodimeric *bc<sub>1</sub>* complex. The *bc<sub>1</sub>* complex features two monomers (A and B), each consisting of one cytochrome *c*<sub>1</sub> (cyt. *c*<sub>1</sub>), one cytochrome *b* (cyt. *b*), and one iron–sulfur protein (ISP) subunit. (b) Each monomer binds four metal centers, heme *c*<sub>1</sub> in the cyt. *c*<sub>1</sub> subunit, and hemes *b*<sub>L</sub> and *b*<sub>H</sub> in the cyt. *b* subunit, while the ISP binds an iron–sulfur ( $\text{Fe}_2\text{S}_2$ ) cluster. The quinol ( $\text{QH}_2$ ) and the quinone (Q) substrate molecules interact with the hemes and the  $\text{Fe}_2\text{S}_2$  cluster to facilitate electron and proton transfers through the complex (A or B) at two distinct binding sites ( $\text{Q}_o$  and  $\text{Q}_i$ ). The arrows indicate schematically pathways of electrons and protons at the initial phase of the Q-cycle. (c) The  $\text{QH}_2$  substrate molecule at the  $\text{Q}_o$ -site of the *bc<sub>1</sub>* complex interacts closely with the H156 residue of the ISP and several other residues of the *bc<sub>1</sub>* complex. The exact binding mode is addressed in the present study.

Figure 1b). Prior to and during the Q-cycle, the substrate molecules  $\text{QH}_2$  and Q bind to the *bc<sub>1</sub>* complex at two distinct sites: the  $\text{Q}_o$ -site captures two  $\text{QH}_2$  and transforms them to Q, while the  $\text{Q}_i$ -site captures one Q and transforms it to  $\text{QH}_2$ . These transformations involve electron and proton exchange between the substrate molecules and the proteins of the *bc<sub>1</sub>* complex.

Even though the mechanism that governs the charge transfer reactions in the Q-cycle has been investigated for decades,<sup>11</sup> the limitations of the experimental techniques and the complexity of the entire process make it difficult to resolve the physicochemical mechanism underlying the Q-cycle. In fact, the individual electron and proton transfer pathways in the *bc<sub>1</sub>* complex are still controversial.<sup>7</sup>

The controversy follows from the following difficulty. The rate-limiting reaction proceeds from an initial complex (the enzyme–substrate complex) formed only under metastable conditions and this complex is by its nature inaccessible to crystallography; indeed, no structures have shown any quinone species in the  $\text{Q}_o$ -site. However, a substantial literature has explored physicochemical parameters for kinetics of the reaction in wildtype and mutant strains, from which a picture of the molecular architecture of the site can be derived.<sup>12–14</sup> In addition, spectroscopic evidence has demonstrated a relatively

stable complex between quinone and the reduced ISP. On the other hand, many structures with quinone analogues bound are available, which show several different configurations for the site, and likely coordinating residues.<sup>15–17</sup>

The electron and proton transfer reactions taking place in the *bc<sub>1</sub>* complex can be resolved into partial processes including intermediate redox and protolytic reactions and chemical states.<sup>18</sup> Technical limitations and the metastable nature of the reaction complex leave many dynamical features inaccessible to direct measurement. For a complete understanding experiment needs to be complemented by computational modeling to identify physicochemical details of the mechanism at the atomistic level. A first attempt to combine crystallographic data with large scale classical molecular dynamics simulations was made early on,<sup>19</sup> but the quantum calculations needed to address the chemistry of catalysis were not feasible at that time. However, computational power is now much improved, and given the central role of the *bc<sub>1</sub>* complex in all respiratory-based bioenergetics, a combined classical and quantum chemical description is a task that should be undertaken with urgency.

Naturally, the experimental–computational studies need to first focus on the initial state with  $\text{QH}_2$  bound to the  $\text{Q}_o$ -site and Q bound to the  $\text{Q}_i$ -site. The redox states of the *bc<sub>1</sub>* complex residues at the  $\text{Q}_o$ - and  $\text{Q}_i$ -sites coordinating initially the substrates are crucial for the Q-cycle, as the coordination and redox states largely influence the rates of electron and proton transfers to and from the substrate molecules. Several coordinating residues of the substrate molecules have been proposed experimentally<sup>20</sup> and have been recently studied through molecular dynamics (MD) simulations.<sup>21</sup> In the case of the  $\text{Q}_o$ -site, the key residue for the binding of  $\text{QH}_2$  is a histidine (H156 in the case of *bc<sub>1</sub>* complex from *Rhodobacter capsulatus*), covalently bonded to the  $\text{Fe}_2\text{S}_2$  cluster of the ISP, as illustrated in Figure 1c. It is assumed that this histidine forms a hydrogen bond with the  $\text{QH}_2$  molecule upon its docking to the  $\text{Q}_o$ -site,<sup>13</sup> thereby keeping the substrate ready for the primary electron and proton transfers.

The chemical specificity of the  $\text{QH}_2$ ···H156 hydrogen bonding is, however, still debated and the actual protonation state of H156 greatly impacts the charge transfer reactions at the  $\text{Q}_o$ -site;<sup>14,22</sup> the protonation state active in normal forward chemistry can be tested by varying environmental pH in the range of the pK of H156 (see also the Supporting Information for a more specific discussion). To establish the binding mode of  $\text{QH}_2$  at the  $\text{Q}_o$ -site, it is, therefore, necessary to consider both protonation states of H156. In addition, one needs to identify other key residues that contribute to the binding of the  $\text{QH}_2$  substrate molecule within the *bc<sub>1</sub>* complex. Particularly important, in this respect, is the inclusion of all charged and polar residues that can potentially contribute to substrate binding at the  $\text{Q}_o$ -site, as these residues can impact critically the rate of electron and proton transfers.

In the present study we investigate, through atomistic molecular dynamics (MD) simulations supported by quantum chemical density functional theory (DFT) calculations, the binding of  $\text{QH}_2$  at the  $\text{Q}_o$ -site of the *bc<sub>1</sub>* complex from *Rhodobacter capsulatus*.<sup>23</sup> The MD simulations were performed for two states of the  $\text{Q}_o$ -site differing in the protonation state of histidine H156. Quantum chemical analysis allowed us to obtain a close view of  $\text{QH}_2$  binding at the  $\text{Q}_o$ -site. The results from the combination of classical and quantum chemical methods provide new insights into the role of the amino acid

residues that hold the QH<sub>2</sub> molecule at the Q<sub>c</sub>-site of the bc<sub>1</sub> complex. The reported findings are consistent with some features of earlier MD simulations,<sup>21</sup> but they identify also rearrangements of binding site residues not discussed previously and investigate two, rather than only one, H156 protonation state. The present study is thus a systematic key first step toward an atomic level investigation of the entire Q<sub>c</sub>-cycle of the bc<sub>1</sub> complex.

## METHODS

We have investigated by means of MD simulation and quantum chemistry calculations two possible binding modes of the QH<sub>2</sub> substrate at the Q<sub>c</sub>-site of the bc<sub>1</sub> complex. The two respective simulations differ in the protonation state of the H156 residue of the ISP (see Figure 1c) that holds QH<sub>2</sub> at the Q<sub>c</sub>-site; H156 was assumed to be either in its protonated (Model I) or in its deprotonated (Model II) form.

MD simulations for the two computational models were performed through NAMD 2.9<sup>24</sup> assuming the CHARMM36 force field with CMAP corrections<sup>25</sup> for the proteins; for lipids and cofactors supplementary force fields<sup>26</sup> were employed, as discussed below. The quantum chemical calculations were carried out with the Gaussian 09 package<sup>27</sup> by using the DFT model chemistry. Analysis of results and snapshots of molecular structures were accomplished with VMD 1.9.1.<sup>28</sup>

**System Preparation.** The simulated systems considered in Models I and II were constructed, using VMD 1.9.1, from the X-ray crystal structure of the bc<sub>1</sub> complex of *Rhodobacter capsulatus* (PDB ID: 1ZRT),<sup>23</sup> embedding the latter in a bilayer membrane, solvating protein and lipids within a TIP3P water box at a salt (NaCl) strength of 0.05 mol/L, and neutralizing the entire system with the salt ions. The bc<sub>1</sub> complex forms a dimeric arrangement of six catalytic subunits,<sup>29</sup> each including cofactors that in the simulations were considered in the oxidized states, as summarized in Table 1.

**Table 1. Oxidation States of the bc<sub>1</sub> Complex Cofactors Assumed in the MD Simulations<sup>a</sup>**

subunit	cofactor	formal charge	oxidation state
cyt. b	heme b <sub>L</sub>	-1	oxidized
	heme b <sub>H</sub>	-1	oxidized
cyt. c <sub>1</sub>	heme c	-1	oxidized
ISP	Fe <sub>2</sub> S <sub>2</sub>	0	oxidized

<sup>a</sup>Cofactors of monomers A and B of the bc<sub>1</sub> complex, shown in Figure 1b, were simulated in identical oxidation states listed for all MD simulations performed.

The assumed oxidized form of all cofactors corresponds to the initial state of the bc<sub>1</sub> complex prior to any charge transfer reaction. Charges and topologies of the bc<sub>1</sub> complex proteins were assumed standard according to the CHARMM36 force field, while parameters for the cofactors were adopted to be consistent with an earlier study<sup>21</sup> and were adopted from an earlier investigation.<sup>26</sup>

Monomers A and B of the bc<sub>1</sub> complex contain a Q<sub>c</sub>-site and a Q<sub>o</sub>-site, where QH<sub>2</sub> and Q substrates become oxidized and reduced, respectively, during the Q<sub>c</sub>-cycle. The 1ZRT crystal structure<sup>23</sup> of the bc<sub>1</sub> complex includes bound stigmatellin molecules at the Q<sub>c</sub>-sites of monomers A and B that were replaced in the performed simulations by QH<sub>2</sub> molecules, aligning for this purpose the QH<sub>2</sub> head groups with the respective head groups of stigmatellin, an approach also used in

an earlier study.<sup>21</sup> The two Q molecules at the Q<sub>c</sub>-sites were placed in the positions of antimycin molecules from the bc<sub>1</sub> complex X-ray crystal structure of wild type *Rhodobacter sphaeroides* (PDB ID: 2QJP), antimycin being added, instead of Q, by the crystallographers for its inhibiting property.<sup>30</sup> Charges and topology of the QH<sub>2</sub> and Q substrates were taken for the present study from an earlier investigation.<sup>26</sup>

The lipid bilayer was modeled as a random distribution of cardiolipin (CL 18:2/18:2/18:2/18:2), phosphatidylcholine (PC 18:2/18:2), and phosphatidylethanolamine (PE 18:2/18:2) lipids, with the concentration matching an earlier simulation;<sup>21</sup> the studied membrane patch included 102 CL, 406 PC, and 342 PE lipids. Since standard CHARMM36 parameters for CL are not available, the force field parameters from a prior study<sup>31</sup> were used for modeling the CL head group, while the parameters for the lipid tails were taken from the standard CHARMM36 force field. For modeling the PE and PC lipids, the standard CHARMM36 force field was employed.<sup>32</sup>

The missing hydrogen atoms from the X-ray structure of the bc<sub>1</sub> complex were reconstructed by using the VMD plugin psfgen.<sup>28</sup> All histidine residues of the bc<sub>1</sub> complex were considered as δ-protonated except for H156, which has been assumed ε-protonated in Model I and deprotonated in Model II. Inspection of the bc<sub>1</sub> complex crystal structure suggested disulfide bonds between the C144 and C167 residues from cyt. c<sub>1</sub>, and between C138 and C155 residues from ISP that were included in the computational models. The simulated system consisted of 502 165 atoms in Model I and 500 791 atoms in Model II, including proteins with cofactors, substrate molecules, lipids, water molecules, and ions.

The H156 residue in the Model II simulation was considered in its deprotonated form and needed to be specifically parametrized as no parameters were available for this residue protonation state in the context of the other residues in the binding site. For this purpose the complex of H156 and the Fe<sub>2</sub>S<sub>2</sub> cluster together with the ligating residues C133, C153, and H135 was optimized using Gaussian 09, employing the B3LYP/6-31G(d) model chemistry.<sup>33</sup> The optimized structure was used to obtain the partial charges, which were determined by means of the electrostatic potential (ESP) fitting procedure;<sup>34</sup> the charges are given in the Supporting Information. The parameters of the bonding, angular, and dihedral interactions for deprotonated H156 were taken from the analogous parameters of the histidine residue in its standard protonation state.

**Molecular Dynamics Simulations.** MD simulations were performed with a time step of 2 fs. Electrostatic and van der Waals interactions were treated with a smooth cutoff of 12 Å. Long-range electrostatic interactions were calculated using the PME method, employing periodic boundary conditions.<sup>35</sup> The equilibration of the system was performed in the NPT ensemble, where the temperature was kept at 310 K by applying to all heavy atoms in the system Langevin forces with a damping coefficient of 5 ps<sup>-1</sup>. Pressure control was achieved during the equilibration simulations through Nosé–Anderson–Langevin piston pressure control<sup>36</sup> at 1 atm, using a piston oscillation period of 200 fs and a damping time scale of 50 fs. The production simulations were carried out in the NVT ensemble.

The protocol of the simulations performed, listed in Table 2, can be subdivided into two parts: (i) system equilibration and (ii) MD simulation. The equilibration was carried out in several

**Table 2. Protocol for *bc*<sub>1</sub> Complex Simulations Carried out in the Present Study<sup>a</sup>**

process	time interval (ns)	
	Model I	Model II
1. equilibration		
structure minimization	50 000 NAMD steps	
lipid bilayer, water molecules and ions released; rest constrained	60 (CH22 + C-H27); 90 (CH36)	
protein side chain released	70	
turns, bridges, and coils motifs released	—	30
all atoms released	60	150
2. MD simulation		
NVT ensemble	360	

<sup>a</sup>Simulations for Model I (502,165 atoms) and Model II (500,791 atoms) of the *bc*<sub>1</sub> complex included an equilibration simulation and a MD simulation for the analysis of QH<sub>2</sub> binding to the Q<sub>o</sub>-site. CH22 + CH27 indicates a combined CHARMM22 and CHARMM27 force field, that was employed initially, while all consecutive simulations were done with the CHARMM36 force field. “NVT ensemble” denotes the canonical ensemble that was employed in MD simulations.

steps. After energy minimization of the initial *bc*<sub>1</sub> structure, lipids, water molecules, and ions were simulated for 60 ns, keeping atoms of the *bc*<sub>1</sub> complex harmonically constrained and employing a combination of CHARMM22 and CHARMM27 force fields. The combination of force fields employed was the same as used in prior MD studies.<sup>21</sup> Following the first 60 ns, a 90 ns simulation with the CHARMM36 force field was performed, still keeping the entire *bc*<sub>1</sub> complex constrained.

Next, the side chains of the *bc*<sub>1</sub> complex were released and the system was equilibrated additionally for 70 ns. Finally, for the Model I simulation, all atoms were released and equilibrated for 60 ns, while for Model II the more flexible motifs of the secondary structure were kept constrained additionally for 30 ns prior to releasing all atoms and performing a 150 ns equilibration of a constraint-free system. After the equilibration, the MD simulation was carried out for 360 ns, for both computational models, in the NVT ensemble.

The duration of the equilibration was guided by monitoring the area of the membrane patch and the root-mean-square deviation (RMSD) of the *bc*<sub>1</sub> complex proteins as these quantities needed to relax to constant values prior to equilibration. The relaxation of membrane patch area and RMSD are shown in the Supporting Information, Figures S2 and S3, respectively, for Model I, and Figures S5 and S6, respectively, for Model II.

**Quantum Chemistry Calculations.** The motif of the Q<sub>o</sub>-site with bound QH<sub>2</sub> was studied using the quantum chemistry package Gaussian 09,<sup>27</sup> employing the UB3LYP DFT method<sup>33</sup> for both Models I and II. This method has been widely used previously in optimizations of iron–sulfur containing systems.<sup>37–43</sup> Two standard 6-311G(d) and 6-311+G(d) basis sets were employed to expand the electronic wave functions. Both methods are of triple- $\zeta$  accuracy, while the latter includes additional diffuse functions.<sup>44</sup> For both Models I and II the quantum chemistry geometry optimizations included the QH<sub>2</sub> head group; pre-equilibrated side chains of residues Y147, I292, E295, and Y302 of cyt. *b*; residues C133, C153, C155, H156, and H135 of ISP; and the Fe<sub>2</sub>S<sub>2</sub> cluster of ISP, thereby, taking into account the major environmental effects that other hybrid methods have included likewise, but through a dielectric model

rather than the explicit treatment of nearby side groups, for studying iron–sulfur cluster containing systems.<sup>22</sup> The structure of the Q<sub>o</sub>-site was studied through quantum chemical energy minimization, where the positions of the C<sub>α</sub> atoms were fixed to positions taken from the pre-equilibrated structure, to avoid an unphysical collapse of the Q<sub>o</sub>-site model. For the quantum chemical calculations the C<sub>α</sub> atoms of the side chain residues were actually replaced by CH<sub>3</sub> groups, employing for this purpose the MOLEFACTURE plugin of VMD.<sup>28</sup>

For Model I, a water molecule has been suggested to play a key role in the binding of the quinol molecule to the Q<sub>o</sub>-site,<sup>21</sup> and was included also in the present quantum chemical calculations; this water molecule is not stably bound in Model II and, hence, not included in this model. The quantum chemical studies for both models included all polar and charged residues at the Q<sub>o</sub>-site and contained approximately 150 atoms.

## RESULTS

The binding of QH<sub>2</sub> to the Q<sub>o</sub>-site of the *bc*<sub>1</sub> complex was characterized first through classical MD simulations. For this purpose the hydrogen bonds that QH<sub>2</sub> forms at the binding site in the course of an MD trajectory were analyzed. This analysis was complemented through calculation of the interaction energy between the QH<sub>2</sub> substrate and *bc*<sub>1</sub> complex residues. The binding of QH<sub>2</sub> at the Q<sub>o</sub>-site was further investigated through quantum chemical calculations accounting for the effect of wide range electron polarization.

**Quinol Binding Motif at the Q<sub>o</sub>-Site.** Based on early crystallographic results,<sup>45</sup> the key residue holding QH<sub>2</sub> at the Q<sub>o</sub>-site is histidine H156 of ISP, shown in Figure 1c. On oxidation of the Fe<sub>2</sub>S<sub>2</sub> cluster, this residue undergoes a dramatic change in pK, from ~12.5 to 7.6, and this allows it to serve as an H-bond acceptor in the bond from QH<sub>2</sub>, thus stabilizing the reaction complex, and initiating the Q-cycle.<sup>14,46–52</sup> Since the protonation state of H156 is still debated,<sup>13,21</sup> two MD simulations were performed, as described in the Methods section, to address QH<sub>2</sub> binding for two suggested<sup>13,21</sup> protonation states of H156.

Figure 2 shows the two binding motifs of QH<sub>2</sub> at the Q<sub>o</sub>-site of the simulated protein–membrane–solvent system. In Model I, shown in Figure 2a, H156 is *c*-protonated and forms a hydrogen bond with its HE2 hydrogen atom to QH<sub>2</sub>, in which the histidine is the H-donor; this hydrogen bond is characterized through the distance d<sub>1</sub>. *c*-protonated H156 also had been assumed in an earlier MD study.<sup>21</sup> In Model II, shown in Figure 2b, H156 is deprotonated and hydrogen bonded to QH<sub>2</sub> through its NE2 nitrogen atom, acting as an H-acceptor. This initial state was also assumed in earlier studies,<sup>53</sup> though with a more truncated quantum chemical model than considered presently.

The simulations show that in Model I a water molecule assumes a stable interaction with QH<sub>2</sub> and links the substrate to the C155 and I292 backbone atoms of the ISP and cyt. *b* subunits, respectively, as illustrated in Figure 2a. The water molecule is only experiencing a stable binding position in the case of the protonated H156 residue; in the case of a deprotonated H156 the water is not present as no stable binding position exists. An earlier MD study<sup>21</sup> demonstrated also stable binding of a water molecule in the case of protonated H156 and proposed that this water molecule is key for proton transfer to the positive side of the membrane.

The QH<sub>2</sub> molecule employs both of its hydroxyl groups in binding to the Q<sub>o</sub>-site; one hydroxyl group binds to H156,

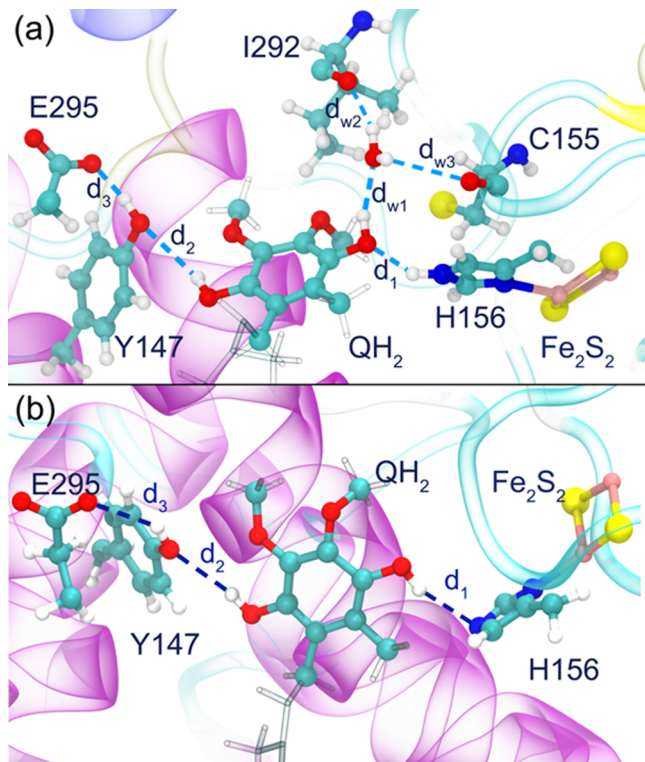


**Figure 2.** Quinol binding at the  $Q_o$ -site of the  $bc_1$  complex. Shown are binding and coordination of  $QH_2$  at the  $Q_o$ -site. Dashed lines represent key hydrogen bonds that coordinate  $QH_2$  to residues H156 and Y147. The labels next to these lines indicate the corresponding bond lengths that are shown in Figure 3 and discussed in the text.  $QH_2$  binding is primarily coordinated through H156, which is in its  $\epsilon$ -protonated form in Model I (a), and in its deprotonated form in Model II (b). In the case of Model I,  $QH_2$  binding is additionally stabilized through a water molecule.

while the other group forms a hydrogen bond with other residues, e.g., with the Y147 and E295 residues of cyt. *b* as shown in Figure 2. The binding of  $QH_2$  to cyt. *b* residues has been extensively studied through the effects of mutation on kinetic and thermodynamic properties, but because the second electron transfer from the  $QH_2$  molecule is not rate limiting, these approaches are less informative than when applied to the first electron transfer. As a consequence, the chemistry of the second electron transfer from the  $QH_2$  is even more controversial.<sup>54</sup> Both  $QH_2$  bindings are important for electron and proton transfers occurring at the  $Q_o$ -site of the  $bc_1$  complex and are, therefore, considered in the present study.

**Analysis of Quinol Bonding at the  $Q_o$ -Site.**  $QH_2$  binding at the  $Q_o$ -site was analyzed by monitoring the lengths of hydrogen bonds formed by the hydroxyl groups of  $QH_2$  with the polar residues of the  $bc_1$  complex. Figure 3 shows the time evolution of these bond lengths calculated for the two monomers of the  $bc_1$  complex for both Model I (blue lines) and Model II (red lines). The insets to the panels introduce atoms participating in the particular bonding.

The time evolution of distance  $d_1$  between the hydroxyl group of  $QH_2$  and the H156 residue is shown in the upper panel of Figure 3. In the case of Model I the bond length  $d_1$  is short throughout the entire 360 ns long simulation, while in the case of Model II this bond length spontaneously increases during the simulation, thereby indicating that  $QH_2$  is more

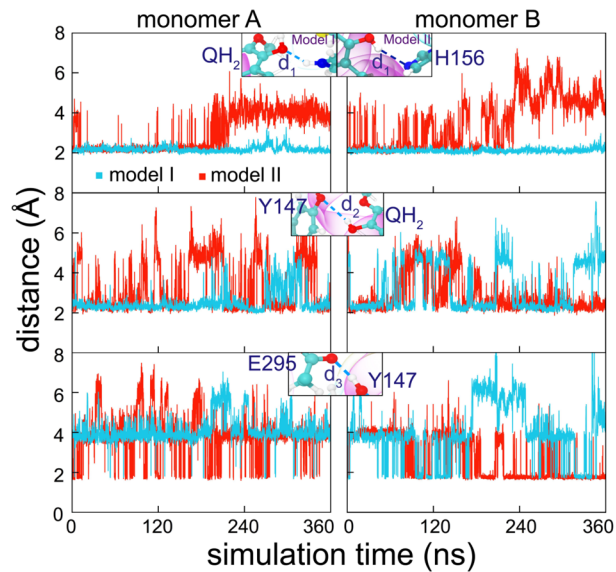


**Figure 3.** Analysis of quinol bonding. Time evolution of the key hydrogen bond lengths stabilizing  $QH_2$  binding at the  $Q_o$ -sites of the  $bc_1$  complex in monomer A (left plots) and B (right plots). Blue lines show the bond lengths calculated for Model I (see Figure 2a), while red lines show the bond lengths for Model II (see Figure 2b). The insets in each panel illustrate the corresponding hydrogen bonding motifs, with lengths labeled  $d_1$ ,  $d_2$ , and  $d_3$ . Bond length  $d_1$  is defined differently in the case of Models I and II.

mobile at the  $Q_o$ -site in the latter case. This behavior is observed for both monomers A and B of the  $bc_1$  complex.

The time evolution of distance  $d_2$ , the hydrogen bond length between hydroxyl groups of  $QH_2$  and the Y147 residue of cyt. *b*, is presented in the middle panels of Figure 3. Our simulations reveal that there arises a hydrogen bond between  $QH_2$  and the Y147 residue in the case of Model I, the bond being less stable in the case of Model II. Indeed, for Model I, the distance  $d_2$  fluctuates around 2.3 Å, with few increases up to ~5 Å. The simulation of Model II also features formation of this hydrogen bond, which, however, is seen to become broken more frequently. The difference in  $d_2$  observed in the two simulations is more profound in monomer A and is very small in monomer B, suggesting, therefore, that spontaneous formation and breaking of the hydrogen bond between the  $QH_2$  molecule and the Y147 residues occurs to a similar degree for Models I and II.

In the course of our MD simulations, the Y147 and E295 side chains rotate such that Y147 comes to lie between  $QH_2$  and E295 and forms hydrogen bonds with the  $-\text{OH}$  of the  $QH_2$  molecule. Formation of such a hydrogen bond between  $QH_2$  and the Y147 residue was unexpected, since this configuration had not been observed in any of the structures. However, because the reaction complex is formed under metastable conditions, a set of forces comes into play that are not explored under crystallographic conditions. Previous studies of  $QH_2$  binding through MD simulation suggested involvement of some water molecules instead.<sup>19,21</sup> In the original X-ray structure of the  $bc_1$  complex the Y147 residue is located far from the  $Q_o$ -site and only in the course of the present MD simulations is this side chain seen to turn and to form a hydrogen bond with  $QH_2$ . Interestingly, in the course of MD equilibration of both Models I and II, the Y147 rotation occurs rapidly after releasing the side chains of the  $bc_1$  complex

proteins, while still keeping backbone atoms constrained; the displacements observed require little movement of the backbone. Formation of the hydrogen bond between QH<sub>2</sub> and the Y147 residue has significant implications on the proton transfer path at the Q<sub>o</sub>-site. Based on the H-bond formed with stigmatellin in all structures with this inhibitor, E295 has previously been considered to be the most likely acceptor of the second proton in the Q<sub>o</sub>-site reaction.<sup>19</sup>

Snapshots from Models I and II MD simulations, featuring hydrogen bonding between Y147 and E295, are shown in Figure 2. In the simulations, the QH<sub>2</sub> molecule forms a hydrogen bond with the Y147 residue, thereby preventing hydrogen bonding between QH<sub>2</sub> and the E295 residue of cyt. *b*, as suggested earlier.<sup>13</sup> Despite the lack of this permanent hydrogen bond, the E295 residue remains located in close proximity to Y147 and our MD simulations reveal that E295 spontaneously forms hydrogen bonds to Y147. The lower panels of Figure 3 show the time dependence of the distance  $d_3$  between the side chains of Y147 and E295. The figure illustrates that for both Models I and II, in either monomer of the bc<sub>1</sub> complex, the distance  $d_3$  is ~3.9 Å, occasionally going down to ~1.8 Å, i.e., to a value typical for a hydrogen bond formed.

**Quinol Stabilization through a Water Molecule.** An important attribute of QH<sub>2</sub> binding to the Q<sub>o</sub>-site in Model I is a water molecule as illustrated in Figure 2a. The water molecule binds to QH<sub>2</sub> and keeps it attached to the I292 and C155 backbone oxygen atoms of cyt. *b* and ISP, respectively. This binding, however, is stable only in the case of Model I, where H156 is protonated.

Stabilization of QH<sub>2</sub> binding at the Q<sub>o</sub>-site through a water molecule can be characterized through hydrogen bonds that the latter forms with QH<sub>2</sub> and surrounding residues. The time evolution of the corresponding bond lengths is shown in Figure 4. The recorded distances,  $d_{w1}$ ,  $d_{w2}$ , and  $d_{w3}$ , in Figure 4 are

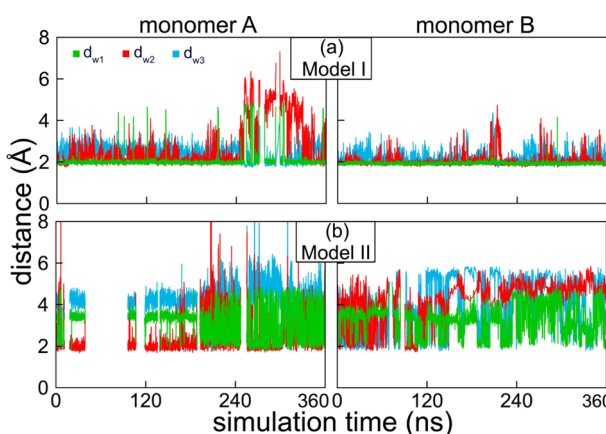


**Figure 4.** Quinol binding at the Q<sub>o</sub>-site coordinated by a water molecule. Shown is the evolution of the lengths of hydrogen bonds formed between QH<sub>2</sub> and a water molecule trapped within monomer A and monomer B of the bc<sub>1</sub> complex. Green lines represent the length  $d_{w1}$  of the bond between the H1 atom of QH<sub>2</sub> and the OH<sub>2</sub> atom of the trapped water molecule, while red and blue lines correspond to the lengths  $d_{w2}$  and  $d_{w3}$  of hydrogen bonds formed between the H1 and H2 atoms of the water molecule and the O atoms of C155 and I292, respectively. The hydrogen bonding network along with  $d_{w1}$ ,  $d_{w2}$  and  $d_{w3}$  are shown in Figure 2a. A water molecule is bound to the QH<sub>2</sub> molecule throughout the entire simulation in the case of Model I (a) and is seen to bind only sporadically in the case of Model II (b).

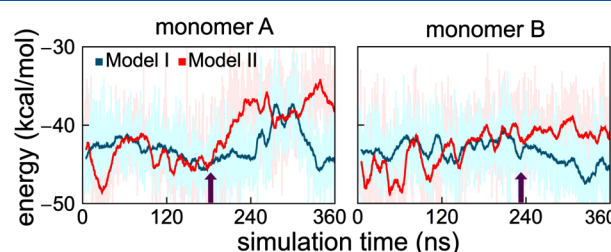
defined in Figure 2a for Model I. Although not shown in Figure 2b, a water in a similar configuration can bind when H156 is deprotonated (Figure 4b for Model II), but with different H-bonding characteristics.

Figure 4a shows that in the case of Model I, in both monomers of the bc<sub>1</sub> complex a water molecule is spontaneously bound to QH<sub>2</sub> as all three distances,  $d_{w1}$ ,  $d_{w2}$ , and  $d_{w3}$ , fluctuate around 2 Å. Only for monomer A  $d_{w3}$  is seen to fluctuate around 2.5 Å, the other two bonds remaining at lower bond length values. Our simulations show that water molecules at the Q<sub>o</sub>-site interchange on a time scale of 15 ps.

The presence of a water molecule at the Q<sub>o</sub>-site, seen in the present simulations, is consistent with an earlier MD simulation.<sup>21</sup> In that study this water molecule was suggested to be important not only because it stabilizes QH<sub>2</sub> binding at the Q<sub>o</sub>-site, but also because it can act as the initial acceptor of a proton from QH<sub>2</sub>, triggering the Q-cycle. The analysis of the hydrogen bond distances performed earlier<sup>21</sup> is fully consistent with the present investigation, thereby validating the present simulation. The analysis of hydrogen bonds associated with a water molecule in Model I indicates that this water molecule acts as a key that fits the space between the QH<sub>2</sub> molecule and the protein's backbone atoms.

In case of Model II, the water molecule is not fitting as a key; the distances  $d_{w1}$ ,  $d_{w2}$ , and  $d_{w3}$  turn out to be significantly different from each other and are not seen to go below 2 Å simultaneously, so that the triple H-bonded configuration of Model I is not seen; the distance  $d_{w1}$  between the QH<sub>2</sub> molecule and a nearby water molecule rarely gets below 2.5 Å and can increase up to 8 Å and even higher. Water molecules occasionally form hydrogen bonds with the backbone oxygen of I292, as illustrated in Figure 4b through the distance  $d_{w2}$ . This observation is, however, likely irrelevant for QH<sub>2</sub> binding as the distances  $d_{w1}$  and  $d_{w3}$  are ~4–5 Å in all cases when  $d_{w2}$  goes below 2 Å. The water molecule, thus, is expected to float around the I292 residue, but not to participate in functional chemistry of the Q<sub>o</sub>-site as it does in the case of Model I.

**Interaction Energy between Quinol and the bc<sub>1</sub> Complex.** The interaction energy of the QH<sub>2</sub> molecule with the bc<sub>1</sub> complex is an important characteristic for QH<sub>2</sub> binding at the Q<sub>o</sub>-site. Figure 5 shows the interaction energy of the QH<sub>2</sub> head group with the rest of the system for Models I and II and for monomers A and B.



**Figure 5.** Quinol interaction with bc<sub>1</sub> complex. Shown is the time evolution of the interaction energy for the QH<sub>2</sub> head group and the rest of the simulated system, including water molecules, lipids, and the bc<sub>1</sub> complex proteins. Blue and red lines show the energies calculated for Models I and II, respectively. The energies calculated for each step of the simulation are shown in shaded colors, while intense color shows a gliding average with energies averaged over a gliding window of 100 ps. Vertical arrows indicate the time instances for monomers A and B, when the QH<sub>2</sub> molecule unbinds from H156 as seen in the Model II simulation.

The interaction energy of  $\text{QH}_2$  with the  $b_{c_1}$  complex in Models I and II fluctuates by about  $\pm 5$  kcal/mol (the value expected for a hydrogen bond) around  $-43$  kcal/mol until the  $\text{QH}_2$  molecule unbinds from the H156 residue. The time instance at which this unbinding occurs is seen in Figure 5 for both monomers of the  $b_{c_1}$  complex.  $\text{QH}_2$  unbinding from H156 is characterized through the distance  $d_1$ , which spontaneously increases from  $2.3$  Å up to  $4.0$  Å in the case of Model II, as illustrated in the upper panels of Figure 3.

The calculated interaction energy of H156 with  $\text{QH}_2$  differs between Models I and II; Figure 5 shows that the energy in Model I is lower than the energy in Model II (accordingly, the binding is stronger), the difference amounting to  $7.8$  kcal/mol for monomer A and  $4.3$  kcal/mol for monomer B. The lower binding affinity of  $\text{QH}_2$  in the case of Model II supports our earlier conclusion that  $\text{QH}_2$  is more mobile at the  $\text{Q}_o$ -site in this case.

We note finally, that in the case of monomer A of Model I there is a short disruption in  $\text{QH}_2$  binding to H156 occurring at  $\sim 240$ – $300$  ns. This disruption is reflected by an increase of the interaction energy of the  $\text{QH}_2$  molecule with the  $b_{c_1}$  complex and is correlated also with a slight increase of the distance  $d_1$  between  $\text{QH}_2$  and H156, as seen in the upper panels of Figure 3.

#### Quantum Chemistry Study of $\text{Q}_o$ -Site Quinol Binding.

The description of  $\text{QH}_2$  binding at the  $\text{Q}_o$ -site of the  $b_{c_1}$  complex by means of classical MD simulations cannot account for polarization of electrons across the binding complex that is expected to contribute to binding strength;<sup>55,56</sup> the participation of electronic degrees of freedom can only be accounted for through quantum chemical calculations. The quantum effects also contribute to the geometry of the binding motif of the  $\text{QH}_2$  molecule at the  $\text{Q}_o$ -site; this contribution was studied for both Models I and II through quantum chemical structure optimization of the  $\text{Q}_o$ -site binding complex. This complex included in our calculation a  $\text{QH}_2$  molecule, the  $\text{Fe}_2\text{S}_2$  cluster of ISP, and several surrounding polar residues that are expected to play a role in primary electron and proton transfer of the  $\text{Q}$ -cycle as highlighted in Figure 6. We note that a similar methodology was successfully applied before to different protein systems.<sup>57–59</sup>

The present choice of the quantum chemistry models is dictated by the electrostatic potential at the  $\text{Q}_o$ -site. Figure 6 shows a characteristic snapshot from the MD simulations of Model I in which the charged and polar amino acid residues can be distinguished from the neutral ones. Figure 6 shows that within a range of about  $10$  Å from the  $\text{QH}_2$  head group only the amino acids H156, H135, E295, Y147, and Y302 should have an impact on  $\text{QH}_2$  binding. Therefore, the side chains of these amino acids were used to construct the quantum mechanical model of the  $\text{Q}_o$ -site. The initial structures of the  $\text{Q}_o$ -site, employed for the quantum chemical studies, were taken from MD simulations for Models I and II, as shown in Figures 7a and 8a, respectively. The details of the optimization protocol are provided in the Methods section.

For the initial geometries of the  $\text{Q}_o$ -site for Models I and II that started the quantum chemical optimizations we selected average postequilibration configurations arising in our MD simulations, as done before.<sup>60,61</sup> Figures 7 and 8 show the initial and optimized geometries of the binding complexes at the  $\text{Q}_o$ -site for Models I and II.

In the course of the quantum chemical optimization of Model I the hydrogen bond network involving the  $\text{QH}_2$

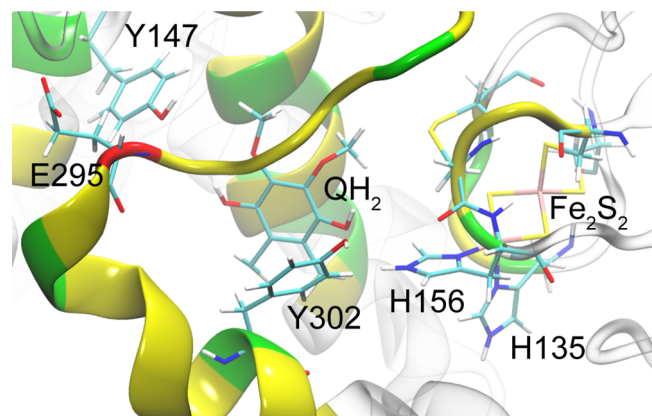


**Figure 6.** Quantum chemistry model of  $\text{QH}_2$  binding at the  $\text{Q}_o$ -site of the  $b_{c_1}$  complex. Included in the quantum chemical description are the components shown here in licorice representation, namely the  $\text{QH}_2$  head group and all residues within  $10$  Å from the head group. The coloring of the  $b_{c_1}$  complex secondary structure illustrates the charge state of the protein amino acids: negative (red), polar uncharged (green), and hydrophobic uncharged (yellow). Side chain groups of polar and negatively charged amino acids surrounding the  $\text{QH}_2$  head group (Y147, H135, H156, E295, Y302) were included into the computational model to describe environmental effects on the  $\text{QH}_2$  binding, while distant charged side chains that point away from the  $\text{QH}_2$  head group and E295 were not included in the quantum chemical description. The  $\text{Fe}_2\text{S}_2$  cluster and all its coordinating amino acids (licorice) have also been included in the computational model.

molecules, the H156 residue, and the water molecule remains largely intact, as a comparison of parts a and b of Figure 7 shows. Indeed, the quantum chemically optimized distance  $d_1$  is  $1.78$  Å, while the average  $\langle d_1 \rangle$  from the MD simulation is  $2.18$  Å. The distances are indicated in Figure 7 and labeled in Figure 2. The distances relevant for  $\text{QH}_2$  binding at the  $\text{Q}_o$ -site are summarized in Table 3. One can see that the distances  $d_{w1}$ ,  $d_{w2}$ , and  $d_{w3}$  for Model I, characterizing positioning of the water molecule discussed above, are also consistent between MD simulations and QM calculations.

The  $\text{Q}_o$ -site geometry optimization for Model I as shown in Figure 7 involves significant rearrangements of residues Y147 and E295 of cyt. *b*. The side chain of residue Y147 turns toward the hydroxyl group of  $\text{QH}_2$  to form a hydrogen bond with it. This turn is accompanied by rearrangement of residue E295, the side chain of which also interacts strongly with Y147. The latter interaction turns out to be so strong that in the course of the quantum chemical optimization procedure the Y147 residue loses its proton and donates it to E295, as seen in Figure 7b.

The rearrangements involving Y147 and E295 are observed both in the quantum chemical optimization and in the classical MD simulations. Table 3 summarizes the mean values of the studied distances, calculated for the entire MD simulation trajectories, as well as values obtained from the corresponding quantum chemistry optimizations. In the case of Model I the distance  $d_2$  becomes as small as  $2.34$  Å, while it fluctuates around a mean value of  $2.52$  Å. The distance  $d_3$  varies around its mean value of  $4.1$  Å in Figure 3, decreasing occasionally to  $1.79$  Å. The spontaneous proton transfer from Y147 to E295, however, cannot arise in an MD simulation, as this process involves breaking of a chemical bond and, therefore, involves electronic degrees of freedom. This explains the discrepancy in the values of distances  $d_2$  and  $d_3$  between the MD simulations and the QM optimization, as listed in Table 3; the quantum

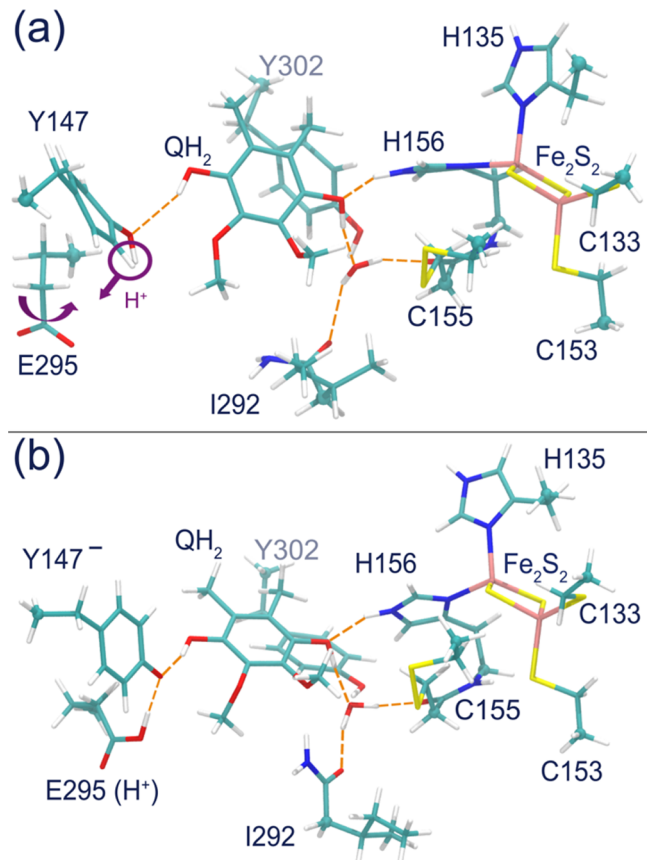


**Figure 7.** Quantum chemical optimization of the binding complex  $\text{Q}_\text{o}$ -site for Model I. Shown are residues of the  $bc_1$  complex directly involved in the binding of  $\text{QH}_2$  at the  $\text{Q}_\text{o}$ -site and covered in our quantum chemistry analysis of Model I. The quantum chemical  $\text{Q}_\text{o}$ -site for Model I includes residues Y147, I292, E295, and Y302 from the cyt. *b* subunit, as well as the  $\text{Fe}_2\text{S}_2$  cluster together with residues C133, C153, C155, H156, and H135 of the ISP subunit. The initial configuration (a) used in the quantum chemical calculations is a conformational average from a  $bc_1$  complex before equilibration. The optimized structure, shown in part b, features rearrangements of residues Y147 and E295 accompanied by spontaneous proton transfer from Y147 to E295. The  $\text{C}_\alpha$  atoms of the amino acid residues (cyan spheres) were fixed during the quantum chemical optimization process.

chemically optimized structure of the  $\text{Q}_\text{o}$ -site reveals that a proton has been transferred from Y147 to E295, while MD simulations show only a rearrangement that makes such a proton transfer possible.

The optimized geometry of the  $\text{Q}_\text{o}$ -site of Model II does not change significantly in the course of the quantum chemical optimization; however, the side chain of residue E295 undergoes a rearrangement. This rearrangement is illustrated in Figure 8 and results in the formation of a hydrogen bond between residues E295 and Y147. The turn of the side chain of E295 for Model II is similar to an analogous rearrangement in Model I; however, no spontaneous proton transfer occurs in the former case. Nevertheless, the H-bonded network is certainly appropriate for proton transfer by a Grotthus-type mechanism, as the bond length of the hydroxyl group of the Y147 side chain has increased by 0.06 Å during the quantum chemical optimization, while  $d_2$  and  $d_3$  decreased by 0.09 and 2.08 Å, respectively. Rearrangement of Y147 and E295 suggests a probable  $\text{QH}_2 \rightarrow \text{Y147} \rightarrow \text{E295}$  path for proton transfer at

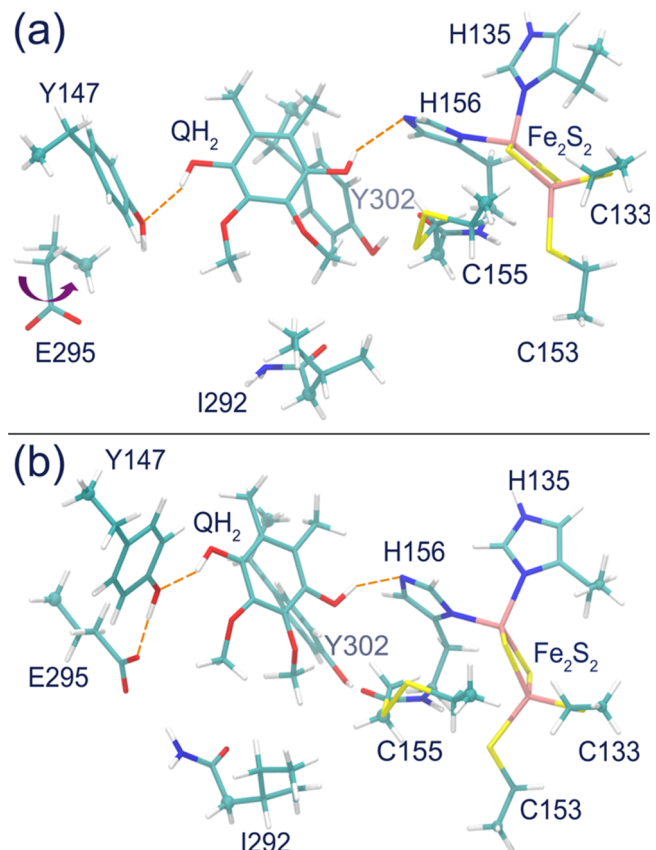


**Figure 8.** Quantum chemical optimization of the  $\text{Q}_\text{o}$ -site binding complex for Model II. Shown are residues of the  $bc_1$  complex directly involved in the binding of the  $\text{QH}_2$  molecule at the  $\text{Q}_\text{o}$ -site and covered in our quantum chemical analysis of Model II. The  $\text{Q}_\text{o}$ -site for Model II is constructed similarly to the  $\text{Q}_\text{o}$ -site for Model I introduced in Figure 7. The key difference here is that residue H156 is deprotonated and that there is no water molecule linking  $\text{QH}_2$  with residues I292 and C155. As in case of Model I, the initial configuration of the  $\text{Q}_\text{o}$ -site used for quantum chemical optimization (a) is a conformational average from a  $bc_1$  complex before equilibration. The optimized structure, shown in part b, features rearrangements of residues Y147 and E295. The  $\text{C}_\alpha$  atoms of the amino acids residues (cyan spheres) were fixed during the quantum chemical optimization process.

the  $\text{Q}_\text{o}$ -site. Such a path had not been discussed earlier, but the strong interaction between the involved residues and the spontaneous proton transfer between Y147 and E295 suggest it.

The comparison of the hydrogen bond lengths in Table 3 reveals that the distance  $d_1$  values, calculated for the  $\text{Q}_\text{o}$ -site through quantum chemical energy optimization and through MD simulations, agree well with each other while the  $\text{QH}_2$  molecule is bound to H156. The distances  $d_2$  and  $d_3$  computed from MD simulations show irregular behavior (see middle and lower panels of Figure 3), and, therefore, their average values are somewhat larger than in the case of a single quantum chemical optimization.

Partial charges and spin density distributions were also analyzed for the quantum chemistry models in order to provide a more accurate description of the  $\text{QH}_2$  binding. For that purpose, both quantum chemistry models were split into 11 fragments as defined in Figure 9. Each atom of the  $\text{Fe}_2\text{S}_2$  cluster was defined as a fragment itself as the iron ions of the cluster should have an antiferromagnetic coupling,<sup>37,44</sup> and it was

Table 3. Hydrogen Bond Lengths at the Q<sub>o</sub>-Site<sup>a</sup>

distances (Å)	bond distance averages (errors) from MD trajectories		bond distances from QMO	
	Model I	Model II	Model I	Model II
$d_1$	2.18 (0.13)	2.31 (0.40), 0–200 ns 3.96 (0.51), 200–360 ns	1.78	1.96
$d_2$	2.52 (0.53)	3.28 (1.26)	1.59	1.91
$d_3$	4.10 (0.67)	3.82 (1.09)	1.02	1.54
$d_{w1}$	2.03 (0.33)		1.75	
$d_{w2}$	2.46 (0.36)		1.80	
$d_{w3}$	2.65 (0.97)		1.73	

<sup>a</sup>Listed are average hydrogen bond lengths calculated from MD trajectories and from QM optimizations (QMO) for Models I and II. The values in parentheses give the standard deviations of the corresponding distances calculated for the 360 ns trajectories (see Table 2). Due to lack of stability a water molecule binding between QH<sub>2</sub> and residues I292 and C155 was not included in the quantum chemical optimization of Model II, and, therefore, the distances  $d_{w1}$ ,  $d_{w2}$ , and  $d_{w3}$  are not given in that case. Since the distance  $d_1$  in Model II experiences a step-wise change (see Figure 3), the average distance value in that case was calculated for the first 200 ns of the MD trajectory. The average value of  $d_1$  for the 200–360 ns interval is 3.96 Å.

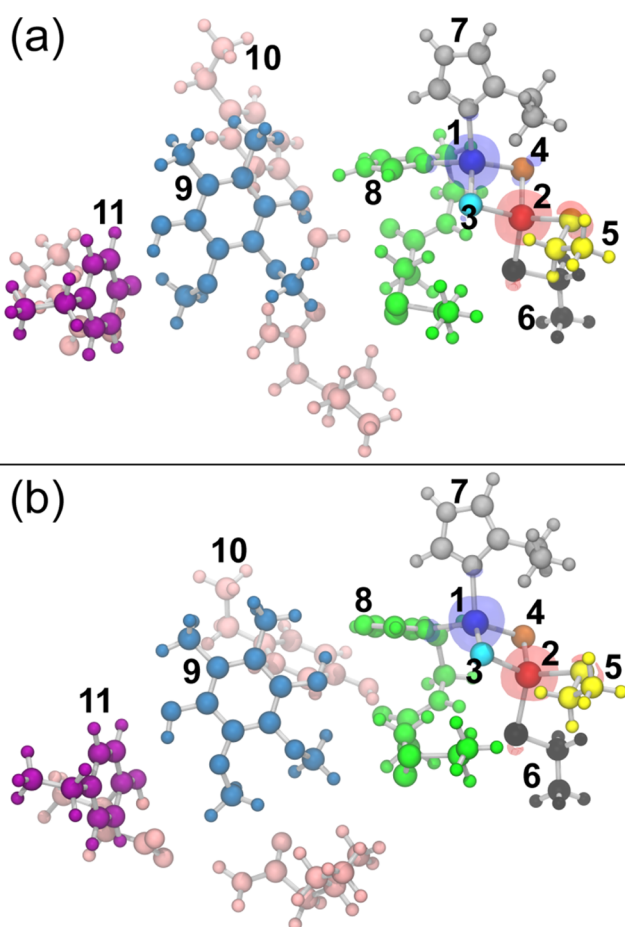


**Figure 9.** Fragments of the Q<sub>o</sub>-site and spin densities. The Q<sub>o</sub>-sites for Models I (a) and II (b) have been subdivided into 11 fragments, whose total charges were analyzed separately and summarized in Table 4. Atoms belonging to a certain fragment are highlighted with the same color. Transparent surfaces around the Fe-atoms show the difference of the total spin density calculated between all  $\alpha$ -electrons (spin up) and all  $\beta$ -electrons (spin down) in the system. The surfaces are shown for the contour values 0.01 (blue) and -0.01 (red) and indicate antiferromagnetic coupling of the two iron ions.

defined so in the calculations. To focus on this coupling, the total difference spin density of the  $\alpha$ -electron spins (spin up) and  $\beta$ -electron spins (spin down) was computed. The spin density difference is illustrated by the distributions obtained

from the quantum chemistry calculations and shown as symmetric transparent surfaces in red and blue in Figure 9.

Table 4 summarizes the partial charges of all fragments (calculated through the Mulliken and ESP-fitted schemes), and the total spin density; the data were obtained by using the B3LYP/6-311G(d) and B3LYP/6-311+G(d) (values in parentheses) methods. It can be noticed that there are some discrepancies between charges calculated with the two methods, mostly for the iron ions, that can be attributed to the additional diffuse functions which are present in the B3LYP/6-311+G(d) computational method. The antiferromagnetic coupling between Fe<sub>A</sub> and Fe<sub>B</sub> ions, however, is still evidenced in both computational approaches; for both Models I and II as seen in Table 4, the spin densities of the iron ions turn out to be around  $\pm 3.8$  (B3LYP/6-311G(d)) and  $\pm 3.4$  (B3LYP/6-311+G(d)).

Although the diffuse functions significantly impact the partial charges of the two iron ions of the Fe<sub>2</sub>S<sub>2</sub> cluster, both DFT methods (B3LYP/6-311G(d) and B3LYP/6-311+G(d)) can still be used to describe QH<sub>2</sub> binding, as follows from the analysis of total charges of the QH<sub>2</sub> and the ISP fragments only. Table 5 summarizes the total charges of the relevant subsystems for the QH<sub>2</sub> binding: the ISP (Fe<sub>2</sub>S<sub>2</sub> cluster and its covalently bonded amino acids), the QH<sub>2</sub> head group, and the environment (involving in the present quantum mechanical calculations all other surrounding amino acids). The comparison of results for both B3LYP/6-311G(d) and B3LYP/6-311+G(d) shows that redistribution of charges in the ISP due to the diffuse functions does not affect the total charge of the ISP subsystems and, therefore, there is no charge delocalization between ISP and QH<sub>2</sub>. Thus, one concludes that deviation of fragment charges seen in Table 4 for the two employed computational methods shows small sensitivity of the Q<sub>o</sub>-site models to the choice of the computational method.

It is important to note that the calculated partial charges of fragments containing Y147 (fragment 11) and E295 (fragment 10), shown in Table 4, clearly indicate that Y147 loses a proton, as the partial charge of fragment 11 (Y147 without its hydroxyl hydrogen) is highly negative. Therefore, one concludes that such transfer occurring during the quantum chemical optimization (see Figure 7) is not a proton coupled electron transfer between these two amino acids. The proton is likely shifted away from Y147 due to the flatness of the potential energy landscape between Y147 and E295. This idea is supported by the quantum chemical optimization results of

**Table 4. Charges and Spin Densities of Q<sub>o</sub>-Site Fragments<sup>a</sup>**

fragment	Mulliken charges		ESP charges		spin densities	
	Model I	Model II	Model I	Model II	Model I	Model II
1: Fe <sub>A</sub>	1.34 (-0.17)	1.37 (-0.25)	0.29 (-0.06)	0.37 (-0.01)	3.82 (3.42)	3.85 (3.40)
2: Fe <sub>B</sub>	1.30 (1.42)	1.30 (1.23)	1.01 (0.74)	1.10 (0.77)	-3.78 (-3.41)	-3.78 (-3.36)
3: S <sub>A</sub>	-1.04 (-0.75)	-1.05 (-0.65)	-0.57 (-0.35)	-0.60 (-0.35)	0.19 (0.27)	0.13 (0.20)
4: S <sub>B</sub>	-0.91 (-0.58)	-0.95 (-0.57)	-0.57 (-0.38)	-0.65 (-0.43)	0.22 (0.33)	0.13 (0.24)
5: C133	-0.48 (-0.48)	-0.54 (-0.53)	-0.39 (-0.32)	-0.47 (-0.40)	-0.31 (-0.38)	-0.28 (-0.33)
6: C153	-0.58 (-0.81)	-0.60 (-0.86)	-0.52 (-0.42)	-0.58 (-0.49)	-0.27 (-0.37)	-0.26 (-0.38)
7: H135	0.13 (0.62)	0.11 (0.56)	0.35 (0.37)	0.35 (0.36)	0.07 (0.08)	0.06 (0.09)
8: H156 + C155	0.18 (0.75)	-0.54 (0.11)	0.34 (0.39)	-0.47 (-0.39)	0.07 (0.06)	0.14 (0.15)
9: QH <sub>2</sub>	-0.09 (-0.11)	-0.11 (-0.04)	-0.08 (-0.21)	-0.05 (-0.06)	0.00 (0.00)	0.00 (0.00)
10: E292 + E295 + Y302 + H <sub>2</sub> O + H <sup>+</sup>	-0.12 (0.01)	-0.41 (-0.37)	-0.04 (0.05)	-0.32 (-0.31)	0.00 (0.00)	0.00 (0.00)
11: Y147 <sup>-</sup>	-0.74 (-0.90)	-0.58 (-0.62)	-0.81 (-0.82)	-0.66 (-0.67)	0.00 (0.00)	0.00 (0.00)

<sup>a</sup>The table summarizes Mulliken charges, ESP-fitted charges, as well as the spin densities of the Q<sub>o</sub>-site fragments calculated with the B3LYP/6-311G(d) and B3LYP/6-311+G(d) methods for Models I and II. The fragments (first column) are defined in Figure 9. Charges and spin densities for each fragment are shown which correspond to the calculations done with the B3LYP/6-311G(d) and B3LYP/6-311+G(d) methods; the values of the B3LYP/6-311+G(d) calculation are given in parentheses. The electronic spin density is defined as the total electron density of electrons of one spin minus the total electron density of the electrons of the opposite spin. The fragments are defined similarly in both models (see Figure 9); however, a water molecule is present in fragment 10 of Model I only, while H156 in fragment 8 is protonated in Model I and deprotonated in Model II. The proton from Y147 (fragment 11) has intentionally been included in fragment 10 to elucidate the charge migration between Y147 and E295.

**Table 5. Total Charges of the Charge Transfer Subsystems of the Q<sub>o</sub>-Site<sup>a</sup>**

fragment	Model I		Model II	
	6-311G(d)	6-311+G(d)	6-311G(d)	6-311+G(d)
ISP	-0.06 (-0.06)	0.00 (-0.03)	-0.90 (-0.95)	-0.96 (-0.94)
QH <sub>2</sub>	-0.09 (-0.08)	-0.11 (-0.21)	-0.11 (-0.05)	-0.04 (-0.06)
environment	-0.86 (-0.85)	-0.89 (-0.77)	-0.95 (-0.98)	-0.99 (-0.98)

<sup>a</sup>Total Mulliken and ESP-fitted charges of the quinol QH<sub>2</sub>, ISP part of the Q<sub>o</sub>-site, and of the remaining system included in the calculations (E292 + E295 + Y302 + Y147). For each fragment the first numbers correspond to the Mulliken charges, while the numbers in parentheses are the ESP-fitted charges. The charges were calculated with the B3LYP/6-311G(d) and B3LYP/6-311+G(d) methods for Models I and II, as indicated.

**Table 6. Total and Interaction Energies of Q<sub>o</sub>-Site Fragments<sup>a</sup>**

fragment	energies	
	Model I	Model II
total energy (au)	-8224.507921 (-8224.633022)	-8147.459089 (-8147.584573)
QH <sub>2</sub> energy (au)	-690.504046 (-690.521193)	-690.506375 (-690.523010)
empty Q <sub>o</sub> energy (au)	-7533.923715 (-7534.043413)	-7456.915233 (-7457.032775)
ΔE (eV)	-2.181 (-1.862)	-1.020 (-0.783)

<sup>a</sup>The energies of the Q<sub>o</sub>-site with the quinol, of the individual quinol QH<sub>2</sub>, and of the empty Q<sub>o</sub>-site were calculated quantum chemically employing the B3LYP/6-311G(d) and B3LYP/6-311+G(d) methods for Models I and II. The energy difference ΔE is the binding energy of the quinol at the Q<sub>o</sub>-site. The B3LYP/6-311+G(d) values are indicated in parentheses.

Model II, in which no proton shift from Y147 to E295 has been observed, despite the similarity of Models I and II. Since the proton can move rather freely between Y147 and E295, it is natural to expect that its exact localization should largely be irrelevant for QH<sub>2</sub> binding to the Q<sub>o</sub>-site.

To study the binding strength of the QH<sub>2</sub> substrate at the Q<sub>o</sub>-site, its interaction energy with the rest of the system was computed. For the subsystems, as defined above, the total energy and QH<sub>2</sub> binding energy are summarized in Table 6. It is important to note that the QH<sub>2</sub> binding in Model I is stronger than in Model II, as also indicated by MD simulations (see Figure 5), and, therefore, in qualitative agreement with the bonding analysis shown in Figure 3. Table 6 also shows that utilization of diffuse functions in the calculations (B3LYP/6-311+G(d) method) consistently lowers the binding energy in both models by approximately 0.3 eV.

## DISCUSSION AND OUTLOOK

The bc<sub>1</sub> complex converts, in the photosynthetic apparatus, the energy available from light harvesting to a proton gradient by using work stored on reduction of Q (quinone) to QH<sub>2</sub> (quinol). Critical for reaching the high efficiency observed in the energy transformation is a bifurcated electron transfer at the Q<sub>o</sub>-site that sends the first electron of a QH<sub>2</sub> substrate to the Fe<sub>2</sub>S<sub>2</sub> center (down in Figure 1a,b) and the second to the Q<sub>c</sub>-site (up in Figure 1a,b), releasing both QH<sub>2</sub> protons to the periplasmic space (in the down-direction of the photosynthetic membrane in Figure 1). The Q thus formed at the Q<sub>o</sub>-site is released, a new QH<sub>2</sub> bound, and the bifurcated reaction undergoes a second cycle. As a result, two electrons are transferred across the membrane up and two electrons are passed via the Fe<sub>2</sub>S<sub>2</sub> center down to cyt. c<sub>2</sub>, the latter shuttling the electrons one-by-one back to the reaction center. Simultaneously, four protons are released on one side (the

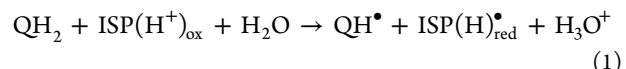
down-side) of the membrane. The electrons transferred to the Q<sub>o</sub>-site reduce a Q bound there to QH<sub>2</sub>, with uptake of two protons from the up-side of the membrane, in effect recycling one of the two QH<sub>2</sub> processed at the Q<sub>o</sub>-site.

Such bifurcated electron transfer along with monodirectional proton transfer requires a reaction complex in which QH<sub>2</sub> binds in a geometrically highly structured site, in which the configuration constrains the reaction coordinate so as to enable productive forward chemistry but minimize the nonproductive bypasses. The structural and kinetic detail needed to establish the mechanism underlying initiation of the Q-cycle requires an approach in which experiment and computational modeling complement each other. Because of the central role of electron and proton transfer processes in the Q-cycle computational modeling has to combine classical molecular dynamics and quantum chemical calculations. The suggestion of the Q-cycle was made already 39 years ago,<sup>62</sup> but only today do we have the computational means available to carry out the quantum chemical calculations needed to demonstrate its detailed structure–function characteristics. In this regard the present study opens a critical new chapter in the field of bioenergetics. Clearly, the starting point of the research needs to be establishment of the QH<sub>2</sub> bound state formed in the Q<sub>o</sub> binding site of the bc<sub>1</sub> complex.

The electrostatic properties of residues forming the Q<sub>o</sub>-site of the bc<sub>1</sub> complex provide an optimal environment for the binding of QH<sub>2</sub> and are responsible for the success of the further redox processes. Thus, the interaction network between QH<sub>2</sub> and some key residues of the bc<sub>1</sub> complex determine the QH<sub>2</sub> binding and the subsequent initiation of the Q-cycle. The results from the MD simulations and the quantum chemistry optimizations in the present investigation have revealed that two binding motifs of the substrate molecule are feasible, namely Models I and II, which differ in the protonation state of ISP residue H156. Experimental results, including pH dependence of the electronic turnover rate,<sup>46,47,63,64</sup> site specific mutagenesis,<sup>14,47,65,66</sup> studies of the thermodynamic cycle,<sup>14,48,67–69</sup> structural,<sup>49,70–72</sup> and spectroscopic studies,<sup>50–52,73,74</sup> have shown that the protonation state of H156 plays a key role in determining the rate of the initial proton-coupled electron transfer reaction at the Q<sub>o</sub>-site. The maximal rates are observed for deprotonated H156, where the oxidized ISP forms a hydrogen bond with the hydroxyl group of the quinol through the N<sub>e</sub> atom (Model II in the present paper). However, the electron turnover is also possible at lower rates,<sup>46,47,63,64</sup> at pH values well below pK<sub>A</sub>, demonstrating that the deprotonated histidine configuration is not essential. In the present study, both protonation states of H156 were considered as they both are supported in the literature.<sup>20,48,74</sup>

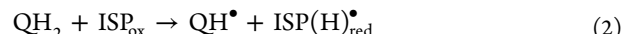
The performed analysis of QH<sub>2</sub> bonding at the Q<sub>o</sub>-site revealed that the substrate molecule forms a hydrogen bonding network, which bridges residues suitable for charge transfer reactions. In this respect, the central role in accommodating QH<sub>2</sub> to the Q<sub>o</sub>-site is played by the H156 residue, as it is involved in the first charge transfer reactions occurring between QH<sub>2</sub> and cyt. c<sub>1</sub>. This residue links the QH<sub>2</sub> substrate molecule and the Fe<sub>2</sub>S<sub>2</sub> cluster of the ISP, and, therefore, operates as an acceptor group which carries the flux of electrons in oxidation of QH<sub>2</sub> by ISP<sub>ox</sub> to generate the intermediate semiquinone. The critical question to be addressed is whether this path also carries the proton flux (Model II), or whether the two charges separate so as to reach the aqueous phase through separate channels (Model I).

Quinol binding in the two computational models (Models I and II) allowed us to identify different scenarios of the primary electron and proton transfer reactions. Thus, in the case of Model I the simulations indicate that the primary proton transfer happens directly to the positive side of the membrane, through a water channel; it follows from the simulations that a water molecule is constantly bound to one of the QH<sub>2</sub> hydroxyl groups through a hydrogen bond, as seen in Figure 2a; the coupled electron and proton transfer reaction in this case is



which corresponds to the configuration assumed in a previous study.<sup>21</sup>

However, in the case of deprotonated H156 (Model II), the QH<sub>2</sub> molecule is expected to donate the proton directly to the H156 residue of the ISP, together with a shift of an electron to the Fe<sub>2</sub>S<sub>2</sub> of the ISP. The reaction describing the charge transfer reaction in this case is simply



where ISP includes both the Fe<sub>2</sub>S<sub>2</sub> cluster and the H156 residue. As previous investigations suggest,<sup>37,44</sup> the two iron ions of the Fe<sub>2</sub>S<sub>2</sub> cluster exhibit anti ferromagnetic coupling. However, such coupling is not explicitly shown in eqs 1 and 2 (spin states of the Fe<sub>2</sub>S<sub>2</sub> cluster ions not specified), as the respective spin state is largely conserved during the proton-coupled electron transfer.

In the present study we have also identified a key role of residues Y147 and E295 in stabilizing QH<sub>2</sub> binding and in providing a possible pathway for the deprotonation of the semiquinone intermediate QH<sup>•</sup> that sets up the reaction complex from which the second electron transfer occurs. A critical consideration in understanding the bifurcated reaction is that of how bypass reactions are minimized. Undesirable bypasses could, in principle, oxidize the semiquinone intermediate without passing its electron to the low potential chain.<sup>75–77</sup> Most interesting from a medical point of view (the bc<sub>1</sub> complex arises also in the respiratory pathway common to most human cells) are reactions leading to reactive oxygen species generated by the semiquinone via reduction of O<sub>2</sub> to the superoxide anion, as such species play a central role in many of the diseases associated with aging, arthritis, or heart disease.<sup>78–80</sup>

Identification of a possible role for Y147 is particularly important because such a role opens possibilities for control of the bifurcation that have not previously been explored.<sup>81</sup> An extensive earlier mutagenesis study<sup>82</sup> of Y147 had concluded that, although this residue serves an important function, the tyrosine hydroxyl group was relatively unimportant, because mutation Y → F gave a strain with about half the activity of wild type. In order to reconcile this finding with the role proposed here, we note that Y147 is not serving as the proton acceptor; that function is served by E295 as suggested earlier.<sup>67,83</sup> Instead, Y147 serves as an intermediary between semiquinone and E295. Although E295 plays a critical role in the second electron transfer through exit of the second proton, the suggested function as a direct ligand stabilizing quinol binding<sup>6,67</sup> is no longer supported.<sup>82,84</sup> This function of Y147 as an intermediary might alternatively be fulfilled by a water bridge, as seen in previous simulations.<sup>21,53</sup> The configuration with a water molecule replacing Y147 might allow the reduced flux seen in the Y → F strain; currently, QM calculations are being

extended to explore the role of water in quinol binding stabilization.

As recognized in other systems,<sup>84</sup> in proton coupled electron transfer processes, the full gamut can be found, depending on how closely the charges are coupled, and the several different examples of such reactions in the  $bc_1$  complex cover a wide range. Although the first electron transfer of the Q-cycle has a special importance as the rate limiting reaction, this feature also means that it is the most accessible to direct kinetic assay. Indeed, the Marcus–Brønsted approach previously developed from kinetic studies<sup>67,82,84</sup> provides a satisfactory model that is compatible with the atomistic picture developed here. The reverse also holds true, namely that the computational approaches pioneered here will be even more essential in studies of less accessible processes.

In contrast to the first step of the Q-cycle, where the electron and proton transfer are likely tightly coupled, in the second step, the charges likely separate so that the electron and proton follow different pathways. The Coulombic consequences provide a rich area for computational investigation. Similarly, many characteristics of the two-electron gate at the Q<sub>o</sub>-site, also proton-coupled electron transfers, remain to be satisfactorily explained. Add to the monomeric processes the complexities of dimeric interactions, and the challenges are exciting. MD can also play a direct role in understanding electron transfer processes.

The two computational models studied here provide insight into the binding of QH<sub>2</sub> at the Q<sub>o</sub>-site of the  $bc_1$  complex. Whereas the key residue for such QH<sub>2</sub> binding, namely H156 of the ISP, is often considered to be in its deprotonated state, our data reveal that a protonated H156 can provide an alternate binding configuration. Because alternative QH<sub>2</sub> binding motifs at the Q<sub>o</sub>-site have now been identified, one should investigate the quantum chemistry of the bifurcated electron transfers from both reaction complexes to ascertain what determines the productive path, and should extend these studies to all reaction pathways for electrons and protons in the Q-cycle. Earlier experimental studies<sup>14,49,51,52,65,67,73,74</sup> already provided some support in favor of the proposed QH<sub>2</sub> binding regimes. With the aim of testing the proposed pathway for forward redox reaction, electron paramagnetic resonance (EPR) measurements can be carried out, since significant accumulation of QH<sup>•</sup> at the Q<sub>o</sub>-site is reached when the second quinol oxidation step is impeded.<sup>83,85,86</sup> Through mutational analysis it might be possible to examine structural associations of QH<sup>•</sup> and ISP(H)<sup>•</sup> and to determine rate constants through rapid-mix freeze-quench EPR. Furthermore, CW-EPR and pulsed EPR approaches can be utilized to measure interactions between QH<sup>•</sup> and ISP(H)<sup>•</sup><sup>87</sup> if both contribute to the product state. The SQ<sub>o</sub> states recently examined<sup>53,85,88</sup> suggest a downstream product, after dissociation. Identification of the intermediate state would allow detailed study of the suggested electron and proton transfer paths. The detailed atomistic analysis performed here can then definitely guide further investigations.

A more profound understanding of the entire  $bc_1$  complex function requires use of highly accurate quantum chemistry methods<sup>89–91</sup> and more extensive MD simulations for identifying possible conformational changes occurring during the Q-cycle. Using the full power of available computational tools in the context of a rich experimental background the inner mechanism of the  $bc_1$  complex, ubiquitous in bioenergetics membranes of the photosynthetic and the respiratory type, should hopefully be revealed.

## ASSOCIATED CONTENT

### S Supporting Information

Experimental insights including the correlation between pK<sub>ox1</sub> and pK<sub>A</sub>, lipid bilayer equilibration, equilibration of the  $bc_1$  complex, equilibration of intermembrane helices, and comparison of quantum chemical optimizations of the Q<sub>o</sub>-site (Figures S1–S8) and the CHARMM topology file, top\_H156.inp, obtained for the MD simulations performed in this study for Model II. This material is available free of charge via the Internet at <http://pubs.acs.org>.

## AUTHOR INFORMATION

### Corresponding Author

\*E-mail: ilia@sdu.dk.

### Notes

The authors declare no competing financial interest.

## ACKNOWLEDGMENTS

The authors acknowledge T. Domratcheva and S. Dikanov for useful discussion on Fe<sub>2</sub>S<sub>2</sub> quantum chemistry. The research reported here has been supported by the National Institutes of Health through grants NIH 9P41GM104601 (to K.S.), NIH 1 R01 GM067887 (to K.S.), and NIH R01 GM35438 (to A.R.C.), the National Science Foundation through grants NSF MCB-120160 (to I.A.S.), NSF MCB-1157615 (to K.S.), and NSF PHY0822613 (to K.S.), and the Russian Scientific Foundation through grant no. 14-12-00342 (to I.A.S.). The authors also acknowledge supercomputer time on Stampede provided by the Texas Advanced Computing Center (TACC) at the University of Texas at Austin through Extreme Science and Engineering Discovery Environment (XSEDE) Grant XSEDE MCA93S028. I.A.S. is grateful for the financial support from the Lundbeck Foundation.

## REFERENCES

- Mitchell, P. D. *Nobel Lectures in Chemistry 1971–1980*; World Scientific Publishing Co.: Hackensack, NJ, 1993.
- Nicholls, D. G.; Ferguson, S. *Bioenergetics*; Academic Press: New York, NY, 2013.
- Wikstrom, M.; Krab, K.; Saraste, M. Proton–Translocating Cytochrome Complexes. *Annu. Rev. Biochem.* **1981**, *50*, 623–655.
- Zhang, Z.; Huang, L.; Shulmeister, V. M.; Chi, Y.-I.; Kim, K. K.; Hung, L.-W.; Crofts, A. R.; Berry, E. A.; Kim, S.-H. Electron Transfer by Domain Movement in Cytochrome bc<sub>1</sub>. *Nature* **1998**, *392*, 677–684.
- Crofts, A. R.; Berry, E. A. Structure and Function of the Cytochrome bc<sub>1</sub> Complex of Mitochondria and Photosynthetic Bacteria. *Curr. Opin. Struct. Biol.* **1998**, *8*, 501–509.
- Mulkidjanian, A. Y. Ubiquinol Oxidation in the Cytochrome bc<sub>1</sub> Complex: Reaction Mechanism and Prevention of Short-circuiting. *Biochim. Biophys. Acta, Bioenerg.* **2005**, *1709*, 5–34.
- Cramer, W. A.; Hasan, S. S.; Yamashita, E. The Q-cycle of Cytochrome bc Complexes: A Structure Perspective. *Biochim. Biophys. Acta, Bioenerg.* **2011**, *1807*, 788–802.
- Xia, D.; Yu, C.-A.; Kim, H.; Xia, J.-Z.; Kachurin, A. M.; Zhang, L.; Yu, L.; Deisenhofer, J. Crystal Structure of the Cytochrome bc<sub>1</sub> Complex from Bovine Heart Mitochondria. *Science* **1997**, *277*, 60–66.
- Lange, C.; Hunte, C. Crystal Structure of the Yeast Cytochrome bc<sub>1</sub> Complex with its Bound Substrate Cytochrome c. *Proc. Natl. Acad. Sci. U.S.A.* **2002**, *99*, 2800–2805.
- Berry, E. A.; Huang, L.-S.; Saechao, L. K.; Pon, N. G.; Valkova-Valchanova, M.; Daldal, F. X-ray Structure of Rhodobacter Capsulatus Cytochrome bc<sub>1</sub>: Comparison with its Mitochondrial and Chloroplast Counterparts. *Photosynth. Res.* **2004**, *81*, 251–275.

- (11) Mitchell, P. Possible Molecular Mechanisms of the Proto-notive Function of Cytochrome Systems. *J. Theor. Biol.* **1976**, *62*, 327–367.
- (12) Gray, K. A.; Davidson, E.; Daldal, F. Mutagenesis of Methionine-183 Drastically Affects the Physicochemical Properties of Cytochrome  $c_1$  of the  $bc_1$  Complex of Rhodobacter capsulatus. *Biochemistry* **1992**, *31*, 11864–11873.
- (13) Crofts, A. R.; Hong, S.; Ugulava, N.; Barquera, B.; Gennis, R.; Guergova-Kuras, M.; Berry, E. A. Pathways for Proton Release During Ubihydroquinone Oxidation by the  $bc_1$  Complex. *Proc. Natl. Acad. Sci. U.S.A.* **1999**, *96*, 10021–10026.
- (14) Lhee, S.; Kolling, D. R.; Nair, S. K.; Dikanov, S. A.; Crofts, A. R. Modifications of Protein Environment of the [2Fe-2S] Cluster of the  $bc_1$  Complex: Effects on the Biophysical Properties of the Rieske Iron-Sulfur Protein and on the Kinetics of the Complex. *J. Biol. Chem.* **2010**, *285*, 9233–9248.
- (15) Gao, X.; Wen, X.; Esser, L.; Quinn, B.; Yu, L.; Yu, C.-A.; Xia, D. Structural Basis for the Quinone Reduction in the  $bc_1$  Complex: A Comparative Analysis of Crystal Structures of Mitochondrial Cytochrome  $bc_1$  with Bound Substrate and Inhibitors at the Qi Site. *Biochemistry* **2003**, *42*, 9067–9080.
- (16) Hunte, C.; Koepke, J.; Lange, C.; Roßmanith, T.; Michel, H. Structure at 2.3 Å Resolution of the Cytochrome  $bc_1$  Complex from the Yeast *Saccharomyces cerevisiae* Co-crystallized with an Antibody Fv Fragment. *Structure* **2000**, *8*, 669–684.
- (17) Ark, G. V.; Berden, J. A. Binding of HQNO to Beef-Heart Sub-mitochondrial Particles. *Biochim. Biophys. Acta, Bioenerg.* **1977**, *459*, 119–137.
- (18) Grimard, V.; Lensink, M.; Debailleul, F.; Ruysschaert, J.-M.; Govaerts, C. *Bacterial Membranes: Structural and Molecular Biology*; Horizon Scientific Press: Wymondham, UK, 2014; Chapter 6.
- (19) Izrailev, S.; Crofts, A. R.; Berry, E. A.; Schulten, K. Steered Molecular Dynamics Simulation of the Rieske Subunit Motion in the Cytochrome  $bc_1$  Complex. *Biophys. J.* **1999**, *77*, 1753–1768.
- (20) Crofts, A. R.; Barquera, B.; Gennis, R. B.; Kuras, R.; Guergova-Kuras, M.; Berry, E. A. Mechanism of Ubiquinol Oxidation by the  $bc_1$  Complex: Different Domains of the Quinol Binding Pocket and Their Role in the Mechanism and Binding of Inhibitors. *Biochemistry* **1999**, *38*, 15807–15826.
- (21) Postila, P. A.; Kaszuba, K.; Sarewicz, M.; Osyczka, A.; Vattulainen, I.; Rög, T. Key Role of Water in Proton Transfer at the Q<sub>o</sub>-Site of the Cytochrome  $bc_1$  Complex Predicted by Atomistic Molecular Dynamics Simulations. *Biochim. Biophys. Acta, Bioenerg.* **2013**, *1827*, 761–768.
- (22) Ullmann, M. G.; Noddleman, L.; Case, D. A. Density Functional Calculation of pKa Values and Redox Potentials in the Bovine Rieske Iron-Sulfur Protein. *J. Biol. Inorg. Chem.* **2002**, *7*, 632–639.
- (23) Berry, E. A.; Huang, L.-S.; Saechao, L. K.; Pon, N. G.; Valkova-Valchanova, M.; Daldal, F. X-ray Structure of *Rhodobacter capsulatus* Cytochrome  $bc_1$ : Comparison with its Mitochondrial and Chloroplast Counterparts. *Photosynth. Res.* **2004**, *81*, 251–275.
- (24) Phillips, J. C.; Braun, R.; Wang, W.; Gumbart, J.; Tajkhorshid, E.; Villa, E.; Chipot, C.; Skeel, R. D.; Kalé, L.; Schulten, K. Scalable Molecular Dynamics with NAMD. *J. Comput. Chem.* **2005**, *26*, 1781–1802.
- (25) Mackerell, A. D.; Feig, M.; Brooks, C. L. Extending the Treatment of Backbone Energetics in Protein Force Fields: Limitations of Gas-Phase Quantum Mechanics in Reproducing Protein Conformational Distributions in Molecular Dynamics Simulations. *J. Comput. Chem.* **2004**, *25*, 1400–1415.
- (26) Kaszuba, K.; Postila, P. A.; Cramariuc, O.; Sarewicz, M.; Osyczka, A.; Vattulainen, I.; Rög, T. Parameterization of the Prosthetic Redox Centers of the Bacterial Cytochrome  $bc_1$  Complex for Atomistic Molecular Dynamics Simulations. *Theor. Chem. Acc.* **2013**, *132*, 1–13.
- (27) Frisch, M. J.; Trucks, G. W.; Schlegel, H. B.; Scuseria, G. E.; Robb, M. A.; Cheeseman, J. R.; Scalmani, G.; Barone, V.; Mennucci, B.; Petersson, G. A. et al. *Gaussian 09*, Revision D.01; Gaussian Inc.: Wallingford, CT, 2009.
- (28) Humphrey, W.; Dalke, A.; Schulten, K. VMD – Visual Molecular Dynamics. *J. Mol. Graphics* **1996**, *14*, 33–38.
- (29) Yang, X.; Trumper, B. Purification of a Three-Subunit Ubiquinol-Cytochrome c Oxidoreductase Complex from *Paracoccus denitrificans*. *J. Biol. Chem.* **1986**, *261*, 12282–12289.
- (30) Esser, L.; Elberry, M.; Zhou, F.; Yu, C.-A.; Yu, L.; Xia, D. Inhibitor-Complexed Structures of the Cytochrome  $bc_1$  from the Photosynthetic Bacterium *Rhodobacter sphaeroides*. *J. Biol. Chem.* **2008**, *283*, 2846–2857.
- (31) Aguayo, D.; González-Nilo, F. D.; Chipot, C. Insight into the Properties of Cardiolipin Containing Bilayers from Molecular Dynamics Simulations, Using a Hybrid All-Atom/United-Atom Force Field. *J. Chem. Theory Comput.* **2012**, *8*, 1765–1773.
- (32) Feller, S. E.; Yin, D.; Pastor, R. W.; MacKerell, A. Molecular Dynamics Simulation of Unsaturated Lipid Bilayers at Low Hydration: Parameterization and Comparison with Diffraction Studies. *Biophys. J.* **1997**, *73*, 2269–2279.
- (33) Becke, A. D. Density-Functional Thermochemistry. III. The Role of Exact Exchange. *J. Chem. Phys.* **1993**, *98*, 5648–5652.
- (34) Bayly, C. I.; Cieplak, P.; Cornell, W.; Kollman, P. A. A Well-Behaved Electrostatic Potential Based Method Using Charge Restraints for Deriving Atomic Charges: the RESP Model. *J. Phys. Chem.* **1993**, *97*, 10269–10280.
- (35) Darden, T.; York, D.; Pedersen, L. Particle Mesh Ewald: An Nlog(N) Method for Ewald Sums in Large Systems. *J. Chem. Phys.* **1993**, *98*, 10089–10092.
- (36) Feller, S. E.; Zhang, Y.; Pastor, R. W.; Brooks, B. R. Constant Pressure Molecular Dynamics Simulation: the Langevin Piston Method. *J. Chem. Phys.* **1995**, *103*, 4613–4621.
- (37) Shoji, M.; Koizumi, K.; Kitagawa, Y.; Yamanaka, S.; Okumura, M.; Yamaguchi, K. Theory of Chemical Bonds in Metalloenzymes IV: Hybrid-DFT Study of Rieske-type [2Fe-2S] Clusters. *Int. J. Quantum Chem.* **2007**, *107*, 609–627.
- (38) Bassan, A.; Blomberg, M. R.; Borowski, T.; Siegbahn, P. E. Oxygen Activation by Rieske Non-heme Iron Oxygenases, a Theoretical Insight. *J. Phys. Chem. B* **2004**, *108*, 13031–13041.
- (39) Salomon, O.; Reiher, M.; Hess, B. A. Assertion and Validation of the Performance of the B3LYP Functional for the First Transition Metal Row and the G2 Test Set. *J. Chem. Phys.* **2002**, *117*, 4729–4737.
- (40) Niu, S.; Nichols, J. A.; Ichijo, T. Optimization of Spin-Unrestricted Density Functional Theory for Redox Properties of Rubredoxin Redox Site Analogues. *J. Chem. Theory Comput.* **2009**, *5*, 1361–1368.
- (41) Sigfridsson, E.; Olsson, M. H.; Ryde, U. A Comparison of the Inner-Sphere Reorganization Energies of Cytochromes, Iron-Sulfur Clusters, and Blue Copper Proteins. *J. Phys. Chem. B* **2001**, *105*, 5546–5552.
- (42) Wilkens, S. J.; Xia, B.; Weinhold, F.; Markley, J. L.; Westler, W. M. NMR Investigations of *Clostridium pasteurianum* Rubredoxin. Origin of hyperfine  $^1\text{H}$ ,  $^2\text{H}$ ,  $^{13}\text{C}$ , and  $^{15}\text{N}$  NMR Chemical Shifts in Iron-Sulfur Proteins as Determined by Comparison of Experimental Data with Hybrid Density Functional Calculations. *J. Am. Chem. Soc.* **1998**, *120*, 4806–4814.
- (43) Sigfridsson, E.; Olsson, M. H.; Ryde, U. Inner-Sphere Reorganization Energy of Iron-Sulfur Clusters Studied with Theoretical Methods. *Inorg. Chem.* **2001**, *40*, 2509–2519.
- (44) Szilagyi, R. K.; Winslow, M. A. On the Accuracy of Density Functional Theory for Iron-Sulfur Clusters. *J. Comput. Chem.* **2006**, *27*, 1385–1397.
- (45) Berry, E. A.; Guergova-Kuras, M.; Huang, L. S.; Crofts, A. R. Structure and function of Cytochrome bc Complexes. *Annu. Rev. Biochem.* **2000**, *69*, 1005–1075.
- (46) Hong, S.; Ugulava, N.; Guergova-Kuras, M.; Crofts, A. R. The Energy Landscape for Ubihydroquinone Oxidation at the Q<sub>o</sub> Site of the  $bc_1$  Complex in *Rhodobacter sphaeroides*. *J. Biol. Chem.* **1999**, *274*, 33931–33944.
- (47) Guergova-Kuras, M.; Kuras, R.; Ugulava, N.; Hadad, I.; Crofts, A. R. Specific Mutagenesis of the Rieske Iron-Sulfur Protein in *Rhodobacter sphaeroides* Shows that both the Thermodynamic

- Gradient and the pK of the Oxidized Form Determine the Rate of Quinol Oxidation by the bc<sub>1</sub> Complex. *Biochemistry* **2000**, *39*, 7436–7444.
- (48) Zu, Y.; Couture, M. M.-J.; Kolling, D. R.; Crofts, A. R.; Eltis, L. D.; Fee, J. A.; Hirst, J. Reduction Potentials of Rieske Clusters: Importance of the Coupling Between Oxidation State and Histidine Protonation State. *Biochemistry* **2003**, *42*, 12400–12408.
- (49) Kolling, D. J.; Brunzelle, J. S.; Lhee, S.; Crofts, A. R.; Nair, S. K. Atomic Resolution Structures of Rieske Iron-Sulfur Protein: Role of Hydrogen Bonds in Tuning the Redox Potential of Iron-Sulfur Clusters. *Structure* **2007**, *15*, 29–38.
- (50) Kolling, D. R.; Samoilova, R. I.; Shubin, A. A.; Crofts, A. R.; Dikanov, S. A. Proton Environment of Reduced Rieske Iron-Sulfur Cluster Probed by Two-Dimensional ESEEM Spectroscopy. *J. Phys. Chem. A* **2008**, *113*, 653–667.
- (51) Hsueh, K.-L.; Westler, W. M.; Markley, J. L. NMR Investigations of the Rieske Protein from Thermus Thermophilus Support a Coupled Proton and Electron Transfer Mechanism. *J. Am. Chem. Soc.* **2010**, *132*, 7908–7918.
- (52) Lin, I.-J.; Chen, Y.; Fee, J. A.; Song, J.; Westler, W. M.; Markley, J. L. Rieske Protein from Thermus thermophilus: <sup>15</sup>N NMR Titration Study Demonstrates the Role of Iron-Ligated Histidines in the pH Dependence of the Reduction Potential. *J. Am. Chem. Soc.* **2006**, *128*, 10672–10673.
- (53) Martin, D. R.; LeBard, D. N.; Matyushov, D. V. Coulomb Soup of Bioenergetics: Electron Transfer in a Bacterial bc<sub>1</sub> Complex. *J. Phys. Chem. Lett.* **2013**, *4*, 3602–3606.
- (54) Saribas, A. S.; Ding, H.; Dutton, P. L.; Daldal, F. Tyrosine 147 of Cytochrome b is Required for Efficient Electron Transfer at the Ubihydroquinone Oxidase Site Q<sub>a</sub> of the Cytochrome bc<sub>1</sub> Complex. *Biochemistry* **1995**, *34*, 16004–16012.
- (55) Hammes-Schiffer, S. Current Theoretical Challenges in Proton–Coupled Electron Transfer: Electron–Proton Nonadiabaticity, Proton Relays, and Ultrafast Dynamics. *J. Phys. Chem. Lett.* **2011**, *2*, 1410–1416.
- (56) Hammes-Schiffer, S. Catalytic Efficiency of Enzymes: A Theoretical Analysis. *Biochemistry* **2013**, *52*, 2012–2020.
- (57) Solov'yov, I. A.; Domratcheva, T.; Moughal Shahi, A. R.; Schulten, K. Decrypting Cryptochrome: Revealing the Molecular Identity of the Photoactivation Reaction. *J. Am. Chem. Soc.* **2012**, *134*, 18046–18052.
- (58) Moughal Shahi, A. R.; Domratcheva, T. Challenges in Computing Electron-Transfer Energies of DNA Repair Using Hybrid QM/MM Models. *J. Chem. Theory Comput.* **2013**, *9*, 4644–4652.
- (59) Solov'yov, I. A.; Domratcheva, T.; Schulten, K. Separation of Photoinduced Radical Pair in Cryptochrome to a Functionally Critical Distance. *Sci. Rep.* **2014**, *4*, 1–8.
- (60) Dittrich, M.; Freddolino, P. L.; Schulten, K. J. When Light Falls in LOV: A Quantum Mechanical/Molecular Mechanical Study of Photoexcitation in Phot-LOV1 of Chlamydomonas reinhardtii. *J. Phys. Chem. B* **2005**, *109*, 13006–13013.
- (61) Zou, X.; Ma, W.; Solov'yov, I. A.; Chipot, C.; Schulten, K. Recognition of Methylated DNA Through Methyl-CpG Binding Domain Proteins. *Nucleic Acids Res.* **2012**, *40*, 2747–2758.
- (62) Mitchell, P. The Protonmotive Q-cycle: A General Formulation. *FEBS Lett.* **1975**, *59*, 137–139.
- (63) Brandt, U.; Okun, J. G. Role of Deprotonation Events in Ubihydroquinone: Cytochrome c Oxidoreductase from Bovine Heart and Yeast Mitochondria. *Biochemistry* **1997**, *36*, 11234–11240.
- (64) Link, T. A.; von Jagow, G. Zinc Ions Inhibit the QP Center of Bovine Heart Mitochondrial bc<sub>1</sub> Complex by Blocking a Protonatable Group. *J. Biol. Chem.* **1995**, *270*, 25001–25006.
- (65) Schröter, T.; Hatzfeld, O. M.; Gemeinhardt, S.; Korn, M.; Friedrich, T.; Ludwig, B.; Link, T. A. Mutational Analysis of Residues Forming Hydrogen Bonds in the Rieske [2Fe-2S] Cluster of the Cytochrome bc<sub>1</sub> Complex in Paracoccus Denitrificans. *Eur. J. Biochem.* **1998**, *255*, 100–106.
- (66) Snyder, C.; Trumppower, B. L. Mechanism of Ubiquinol Oxidation by the Cytochrome bc<sub>1</sub> Complex: Pre-steady-state Kinetics of Cytochrome bc<sub>1</sub> Complexes Containing Site-Directed Mutants of the Rieske Iron-Sulfur Protein. *Biochim. Biophys. Acta, Bioenerg.* **1998**, *1365*, 125–134.
- (67) Crofts, A. R. Proton-coupled Electron Transfer at the Q<sub>a</sub>-site of the bc<sub>1</sub> Complex Controls the Rate of Ubihydroquinone Oxidation. *Biochim. Biophys. Acta, Bioenerg.* **2004**, *1655*, 77–92.
- (68) Link, T. A. Two pK Values of the Oxidised Rieske [2Fe-2S] Cluster Observed by CD Spectroscopy. *Biochim. Biophys. Acta, Bioenerg.* **1994**, *1185*, 81–84.
- (69) Leggate, E. J.; Hirst, J. Roles of the Disulfide Bond and Adjacent Residues in Determining the Reduction Potentials and Stabilities of Respiratory-type Rieske Clusters. *Biochemistry* **2005**, *44*, 7048–7058.
- (70) Iwata, S.; Saynovits, M.; Link, T. A.; Michel, H. Structure of a Water Soluble Fragment of the Rieske Iron–Sulfur Protein of the Bovine Heart Mitochondrial Cytochrome bc<sub>1</sub> Complex Determined by MAD Phasing at 1.5 Å Resolution. *Structure* **1996**, *4*, S67–S79.
- (71) Colbert, C. L.; Couture, M. M.-J.; Eltis, L. D.; Bolin, J. T. A Cluster Exposed: Structure of the Rieske Ferredoxin From Biphenyl Dioxygenase and the Redox Properties of Rieske Fe-S proteins. *Structure* **2000**, *8*, 1267–1278.
- (72) Hunsicker-Wang, L. M.; Heine, A.; Chen, Y.; Luna, E. P.; Todaro, T.; Zhang, Y. M.; Williams, P. A.; McRee, D. E.; Hirst, J.; Stout, C. D.; et al. A Cluster Exposed: Structure of the Rieske Ferredoxin From Biphenyl Dioxygenase and the Redox Properties of Rieske Fe-S Proteins. *Biochemistry* **2003**, *42*, 7303–731.
- (73) Dikanov, S. A.; Kolling, D. R.; Endewerd, B.; Samoilova, R. I.; Prisner, T. F.; Nair, S. K.; Crofts, A. R. Identification of Hydrogen Bonds to the Rieske Cluster Through the Weakly Coupled Nitrogens Detected by Electron Spin Echo Envelope Modulation Spectroscopy. *J. Biol. Chem.* **2006**, *281*, 27416–27425.
- (74) Iwaki, M.; Yakovlev, G.; Hirst, J.; Osyczka, A.; Dutton, P. L.; Marshall, D.; Rich, P. R. Direct Observation of Redox-Linked Histidine Protonation Changes in the Iron-Sulfur Protein of the Cytochrome bc<sub>1</sub> Complex by ATR-FTIR Spectroscopy. *Biochemistry* **2005**, *44*, 4230–4237.
- (75) Boveris, A. Determination of the Production of Superoxide Radicals and Hydrogen Peroxide in Mitochondria. *Methods Enzymol.* **1984**, *105*, 429–435.
- (76) Muller, F. The Nature and Mechanism of Superoxide Production by the Electron Transport Chain: its Relevance to Aging. *J. Am. Aging Assoc.* **2000**, *23*, 227–253.
- (77) Turrens, J. F.; Alexandre, A.; Lehninger, A. L. Ubisemiquinone is the Electron Donor for Superoxide Formation by Complex III of Heart Mitochondria. *Arch. Biochem. Biophys.* **1985**, *237*, 408–414.
- (78) Beckman, K. B.; Ames, B. N. The Free Radical Theory of Aging Matures. *Physiol. Rev.* **1998**, *78*, 547–581.
- (79) Harman, D. Free Radical Theory of Aging. *Mutat. Res.* **1992**, *275*, 257–266.
- (80) Muller, F. L.; Lustgarten, M. S.; Jang, Y.; Richardson, A.; Van Remmen, H. Trends in Oxidative Aging Theories. *Free Radical Biol. Med.* **2007**, *43*, 477–503.
- (81) Crofts, A. R.; Hong, S.; Wilson, C.; Burton, R.; Victoria, D.; Harrison, C.; Schulten, K. The Mechanism of Ubihydroquinone Oxidation at the Q<sub>a</sub>-site of the Cytochrome bc<sub>1</sub> Complex. *Biochim. Biophys. Acta, Bioenerg.* **2013**, *1827*, 1362–1377.
- (82) LeBard, D. N.; Matyushov, D. V. Protein–Water Electrostatics and Principles of Bioenergetics. *Phys. Chem. Chem. Phys.* **2010**, *12*, 15335–15348.
- (83) Victoria, D.; Burton, R.; Crofts, A. R. Role of the -PEWY-Glutamate in Catalysis at the Q<sub>a</sub>-site of the Cyt bc<sub>1</sub> Complex. *Biochim. Biophys. Acta, Bioenerg.* **2013**, *1827*, 365–386.
- (84) Hammes-Schiffer, S.; Soudackov, A. V. Proton–Coupled Electron Transfer in Solution, Proteins, and Electrochemistry. *J. Phys. Chem. B* **2008**, *112*, 14108–14123.
- (85) Cape, J. L.; Bowman, M. K.; Kramer, D. M. A Semiquinone Intermediate Generated at the Q<sub>a</sub> site of the Cytochrome bc<sub>1</sub> Complex: Importance for the Q-cycle and Superoxide Production. *Proc. Natl. Acad. Sci. U.S.A.* **2007**, *104*, 7887–7892.

- (86) Zhang, H.; Oszczka, A.; Dutton, P. L.; Moser, C. C. Exposing the Complex III Q<sub>o</sub> Semiquinone Radical. *Biochim. Biophys. Acta, Bioenerg.* **2007**, *1767*, 883–887.
- (87) Cammack, R.; MacMillan, F. *Metals in Biology*; Springer: Secaucus, NJ, 2010; pp 11–44.
- (88) Vennam, P. R.; Fisher, N.; Krzyaniak, M. D.; Kramer, D. M.; Bowman, M. K. A caged, destabilized free radical intermediate in the Q-Cycle. *Chem. Biochem.* **2013**, *14*, 1745–1753.
- (89) Eriksen, J.; Sauer, S.; Mikkelsen, K.; Jensen, H.; Kongsted, J. On the Importance of Excited State Dynamic Response Electron Correlation in Polarizable Embedding Methods. *J. Comput. Chem.* **2012**, *33*, 2012–2022.
- (90) Knecht, S.; Marian, C.; Kongsted, J.; Mennucci, B. On the Photophysics of Carotenoids: A Multireference DFT Study of Peridinin. *J. Phys. Chem. B* **2013**, *117*, 13808–13815.
- (91) Beerepoot, M.; Steindal, A.; Kongsted, J.; Brandsdal, B.; Frediani, L.; Ruud, K.; Olsen, J. A Polarizable Embedding DFT Study of One-Photon Absorption in Fluorescent Proteins. *Phys. Chem. Chem. Phys.* **2013**, *15*, 4735–4743.